Proceedings of the 2000 U.S. DOE Hydrogen Program Review
NREL/CP-570-28890

Modeling of dense gas-solid reactive mixtures applied to biomass pyrolysis in a fluidized bed

D. Lathouwers and J. Bellan
Jet Propulsion Laboratory
California Institute of Technology
Pasadena, CA 91109

Abstract

A model is presented for mathematically describing the thermo fluid dynamics of dense, reactive, gas-solid mixtures. The model distinguishes among multiple particle classes, either on the basis of their physical properties (diameter, density) or through their thermo-chemistry (reactive vs. inert particles). A multifluid approach is followed where macroscopic equations are derived from the kinetic theory of granular flows using inelastic rigid-sphere models, thereby accounting for collisional transfer in high-density regions. Separate transport equations are constructed for each of the particle classes, allowing for the description of the independent acceleration of the particles in each class and the interaction between size classes, as well as for the equilibration processes whereby momentum and energy are exchanged between the respective classes and the carrier gas. Aimed at high density suspensions, such as fluidized beds, the relations obtained for the stress tensor are augmented by a model for frictional transfer, suitably extended to multiple-class systems. Although applicable to general gas-solid combustion systems, the model is combined here with a detailed, separately validated, chemistry model describing the pyrolysis of biomass particles. The noteworthy novelties of the model include: (i) a systematic and consistent derivation of the solids transport equations and transport properties within the multifluid concept, allowing for non-equilibrium effects between the respective particle classes, (ii) the ability to explicitly account for the possibility of porous solid fuel particles, and (iii) the modeling of multiple chemical reactions in both gas and solid phases and the associated effects of heat and mass transfer. The model is applied to high-temperature biomass particle pyrolysis in a lab-scale fluidized bed reactor and is evaluated on comparing yield of reaction products. The results indicate that the gas temperature is the foremost parameter influencing tar yield. The biomass feed temperature, the nature of the feedstock, and the fluididization velocity, all have minor impact on the yield. It is also shown that the gas temperature can be optimized for maximizing the tar yield.

Contents

1 Introduction

Many practical multiphase flow systems involve the flow of a dense, reactive, gas-particle mixture. Examples include coal combustion, catalyst regeneration and pyrolysis applications, among others. Because of the lack of fundamental knowledge of both the fluid-mechanical and thermal behavior of these systems, the design of these processes has been necessarily based on empirical correlations and experiments performed in laboratory or pilot scale units. However, models and simulations of these systems would allow the optimization of the processes and their scaling, without the need for expensive and time consuming testing. This work is the first step towards providing such a model.

One of the distinctive characteristics of these dense flows is that momentum and energy are primarily exchanged through collisions between particles rather than through the gaseous phase (Savage and Sayed, 1984). The particles then interact similarly to the molecules of a dense gas. Jenkins and Savage (1983) first exploited this analogy and used a kinetic theory approach, based on Gaussian velocity distributions, to derive macroscopic equations of the mixture. Since then, this concept has been expanded and improved by considering more general velocity distributions (Lun et al., 1984; Jenkins and Richman, 1985), important for more dilute regions, and by including effects of the interstitial gas (e.g. Balzer et al., 1993), which may be important for small particles. A crucial role in these theories is played by the 'granular temperature', the mean kinetic energy associated with the velocity fluctuations of the particles. Reviews on granular flows are given by Campbell (1990) and Goldhirsch (1999).

Most of the modeling work performed so far has focussed on isothermal, monodisperse mixtures. The majority of industrial interest, however, lies in systems that include multiple particle types and reactive flows, with their associated effects of mixing, segregation and heat transfer (see the recent review of Ottino and Khakhar, 2000 for segregation phenomena). Analyses of binary (or multicomponent) dry granular mixtures are available (Farell et al., 1986; Jenkins and Mancini, 1987; Jenkins and Mancini, 1989; Zamankhan, 1995), and are based on extensions of standard kinetic theory of dense gases (e.g. Tham and Gubbins, 1971), appropriately modified to include the effect of dissipation due to inelasticity. In all of the aforementioned references, equipartition of granular energy of the respective particle classes is assumed. However, this assumption holds for molecular systems where dissipative effects are absent, and when the mass ratio of the respective particles is moderate. For granular flows, this assumption is inappropriate due to the dissipation associated with the inelasticity of particle collisions. Furthermore, all aforementioned studies assume the drift velocity between the respective particle classes to be small compared to a representative velocity of particle fluctuation, an assumption that is inappropriate for more dilute granular systems subject to body forces, causing appreciable drift (Gourdel et al., 2000).

The theoretical investigation of heat transfer in granular systems has been initiated only recently. Louge et al. (1993) investigated the thermal behavior of a dilute suspension whereas Hsiau (2000) has given a detailed analysis of the heat transfer coefficient for a wide region of particle fractions, both for monodisperse and for binary mixtures. Theoretical foundations on dense, reactive multicomponent, mixtures, where all of the above processes play a role, are virtually absent in literature.

In the present study, we derive a comprehensive model for the flow of a multicomponent, dense, reactive, particle mixture. To this end, separate dynamic equations are derived for each particle class describing the evolution of its mean velocity, temperature, etc. These transport equations are coupled through source terms that describe the various non-equilibrium processes, such as mass, momentum and energy transfer, both between particles and the gas, and between the respective particle classes. The kinetic theory is based on a Gaussian approximation for the velocity distribution, assuming the spatial gradients of the mean variables to be small and the particles to be nearly elastic. Detailed analysis of the heat transfer during a collision between particles indicates that this constitutes a negligible contribution, and consequently the conduction in the particle phases is treated as a self-diffusion phenomenon, based on the recent analysis given by Hsiau (2000). Other diffusive contributions, resulting from the random motion of the particles are modeled in a similar way. The source terms expressing the transfer mechanisms are obtained by averaging the appropriate transfer correlations for a single particle.

As an application of the present work, the hydrodynamic equations are combined with a validated chemistry model for the description of biomass particle pyrolysis, consisting of 7 solid species and 2 gaseous components. The complete model is then applied to the pyrolysis in a pilot-scale fluidized bed and compared to appropriate experimental data of specific product yields.

2 Mathematical model

A continuum model is derived by applying separate averaging procedures for both the carrier gas and solid phases. A phase ensemble average is used for the carrier phase, combined with a particle ensemble average where particle properties, such as velocity, are directly averaged. This is attractive when resolution of the detailed degrees of freedom of the particles (e.g. internal temperature profiles or profiles of the internal chemical composition) is undesirable or unnecessary.

2.1 Single particle biomass pyrolysis model

The particle pyrolysis model employed here is that of the detailed kinetics derived by Miller and Bellan (1997), based on superimposed cellulose, hemicellulose, and lignin reactions. This enables the simulation of different biomass feedstock through knowledge of the initial mass composition with respect to these three primary components; biomass impurities are lumped with the hemicellulose as this model correlated best with the experimental data. Each of the virgin components undergoes the same generic competitive reaction scheme:

$$\begin{aligned}
&\text{virgin}(s) \xrightarrow{K_1} \text{active}(s)\\
&\text{active}(s) \xrightarrow{K_2} \text{tar}(g)\\
&\text{active}(s) \xrightarrow{K_3} X\text{char}(s) + (1-X)\text{gas}(g)\\
&\text{tar}(g) \xrightarrow{K_4} \text{gas}(g)
\end{aligned}$$

As indicated in the above kinetics scheme, the virgin components, the active intermediates and the char are solid phase species, while tar and gas are vapor products; these species are not pure chemical species but represent groups of compounds. All reactions are modelled with first order Arrhenius kinetics; $K_i = A_i \exp(-E_i/RT)$, where the rate constants, A_i, activation energies, E_i for reactions K_1, K_2, K_3 and the mass ratio X are dependent on the particular component, whereas all heats of reaction and secondary tar decomposition parameters (K_4) are independent of the source component.

This kinetics model combined with a porous particle flow dynamics model yielded validated predictions on tar/char yields ranging from the kinetically controlled region (micro particles) to the diffusion controlled limit (macro particles), cf. Miller and Bellan (1997). In the present paper, for simplicity, the biomass pyrolysis is assumed kinetically controlled. This assumption may be justified in the dense particulate regime where contact between particles may induce fragmentation (see Miller and Bellan, 1998, for a fragmentation model) and reduce the size of the particles to the point where the internal temperature equilibrates rapidly. Thus, the particle temperature, its mass and composition (global solid mass fractions) completely describe the state of the particle.

The sand and biomass particles are both solid and hence thermodynamically belong to the same phase. They, however, have different physical properties and different temperatures, etc. In particular, the biomass particles are porous whereas the sand particles are not. Therefore these particle classes are handled separately.

2.2 Gas phase transport equations

As the procedure for phase ensemble averaging is well-known (Drew, 1983), we will restrict the present discussion to the necessary results. The general ensemble average of a field quantity $\Psi(\mathbf{x}, t)$, ($\mathbf{x}, t$ denoting space and time coordinates) is

$$< \Psi(\mathbf{x}, t) >= \int \Psi(\mathbf{x}, t) P(\omega) d\omega \qquad (1)$$

where $P(\omega)$ is the probability that a specific realization ω is encountered in the ensemble. The gas-phase ensemble average and its density-weighted counterpart are defined Drew (1983) as $\overline{\Psi} \equiv < \chi_g \Psi(\mathbf{x}, t) > / \alpha_g$ and $\widetilde{\Psi} \equiv < \chi_g \rho_g \Psi(\mathbf{x}, t) > / \alpha_g \overline{\rho}_g$, where ρ_g is the gas density, χ_g denotes the phase indicator of the gas phase which is unity in the gas phase and zero otherwise, and the gas phase fraction, α_g, is defined as the ensemble average of the indicator function, i.e. $\alpha_g =< \chi_g >$. The average transport equations for the gas phase now follow by multiplying the local instantaneous equations (the Navier Stokes set supplemented with energy and species equations) by the phase indicator and ensemble averaging:

$$\begin{aligned}
\frac{\partial(\alpha\overline{\rho})_g}{\partial t} + \nabla \cdot (\alpha\overline{\rho}\widetilde{\mathbf{u}})_g &= \Gamma_g && (2)\\
\frac{\partial(\alpha\overline{\rho}\mathbf{u})_g}{\partial t} + \nabla \cdot (\alpha\overline{\rho}\widetilde{\mathbf{u}}\widetilde{\mathbf{u}})_g &= \nabla \cdot \alpha[-\overline{p} + \overline{\boldsymbol{\tau}} + \boldsymbol{\Sigma}_g^{\mathrm{Re}}]_g + \alpha_g\overline{\rho}_g\mathbf{f}_g + \mathbf{M}_g + \Gamma_g\mathbf{u}_g^i && (3)\\
\frac{\partial(\alpha\rho\widetilde{h})_g}{\partial t} + \nabla \cdot (\alpha\overline{\rho}\widetilde{\mathbf{u}}\widetilde{h})_g &= -\nabla \cdot \alpha[\overline{\mathbf{q}} + \mathbf{q}^{\mathrm{Re}}]_g + F_g + \Gamma_g h_g^i && (4)\\
\frac{\partial(\alpha\overline{\rho}\widetilde{Y}_\xi)_g}{\partial t} + \nabla \cdot (\alpha\overline{\rho}\widetilde{\mathbf{u}}\widetilde{Y}_\xi)_g &= -\nabla \cdot \alpha[\overline{\mathbf{j}}_{g\xi} + \mathbf{j}_\xi^{\mathrm{Re}}]_g + \alpha_g\overline{\rho}_g\widetilde{R}_{g\xi} + H_{g\xi} + \Gamma_g Y_{g\xi}^i. && (5)
\end{aligned}$$

Here, the main variables are the gas velocity $\mathbf{u}$, the specific enthalpy h, the gas pressure p, and the mass fractions of specie $_\xi$, Y_ξ. $\boldsymbol{\tau}$, $\mathbf{q}$, and $\mathbf{j}_{g\xi}$ denote the molecular viscous stress, the molecular heat flux vector and the species diffusion flux vector, respectively. The gravitational acceleration is given by $\mathbf{f}_g$, and $R_{g\xi}$ is the reaction rate for specie ξ. The terms $\mathbf{M}_g$, F_g, and $H_{g\xi}$ denote the diffusive interfacial transfer of momentum, enthalpy and species mass, respectively, and are defined as

$$\mathbf{M}_g \equiv - < (-p + \boldsymbol{\tau}) \cdot \nabla\chi_g >; H_{g\xi} \equiv < \mathbf{j}_{g\xi} \cdot \nabla\chi_g >; F_g \equiv < \mathbf{q}_g \cdot \nabla\chi_g > . \tag{6}$$

The terms Γ_g, $\Gamma_g\mathbf{u}_g^i$, $\Gamma_g Y_{g\xi}^i$, and $\Gamma_g h_g^i$ are the convective interfacial transfer fluxes of mass, momentum, enthalpy and species mass, and are expressed in terms of the gas velocity at the interface between the phases, $\mathbf{u}_{gi}$

$$\begin{aligned}
\Gamma_g &\equiv < \rho_g(\mathbf{u}_g - \mathbf{u}_{gi}) \cdot \nabla\chi_g > && (7)\\
\Gamma_g\mathbf{u}_g^i &\equiv < \rho_g\mathbf{u}_g(\mathbf{u}_g - \mathbf{u}_{gi}) \cdot \nabla\chi_g > && (8)\\
\Gamma_g Y_{g\xi}^i &\equiv < \rho_g Y_{g\xi}(\mathbf{u}_g - \mathbf{u}_{gi}) \cdot \nabla\chi_g > && (9)\\
\Gamma_g h_g^i &\equiv < \rho_g h_g(\mathbf{u}_g - \mathbf{u}_{gi}) \cdot \nabla\chi_g > . && (10)
\end{aligned}$$

Finally, the equations contain 'turbulent' fluxes, $\boldsymbol{\Sigma}_g^{\mathrm{Re}}$, $\mathbf{j}_{g\xi}^{\mathrm{Re}}$, $\mathbf{q}_g^{\mathrm{Re}}$ expressing the flux of momentum, enthalpy and species mass given by the following expressions

$$\boldsymbol{\Sigma}_g^{\mathrm{Re}} \equiv -\frac{< \chi_g\rho_g\mathbf{u}_g'\mathbf{u}_g' >}{\alpha_g}; \mathbf{j}_{g\xi}^{\mathrm{Re}} \equiv \frac{< \chi_g\rho_g\mathbf{u}_g' Y_{g\xi}' >}{\alpha_g}; \mathbf{q}_g^{\mathrm{Re}} \equiv \frac{< \chi_g\rho_g\mathbf{u}_g' h_g' >}{\alpha_g}, \tag{11}$$

where the fluctuations result from a decomposition of each of the instantaneous variables into its mean and a fluctuation, e.g. $\mathbf{u}_g = \widetilde{\mathbf{u}}_g + \mathbf{u}_g'$. A detailed turbulence model derivation for the general reactive case can be found in Lathouwers and Bellan (1999b). Owing to the usage of appropriate density-weighted variables, the general form of these transport equations is comparable to their local instantaneous form. In the above enthalpy equation, we have neglected the effect of pressure work and viscous dissipation.

Neglecting correlations between the gas temperature and mass fractions gives the averaged equations of state

$$\overline{p}_g = R^0 \overline{\rho}_g \sum_{\xi} \frac{\widetilde{Y}_\xi}{W_\xi} \widetilde{T}_g \tag{12}$$

where R^0 denotes the universal gas constant, W_ξ is the molecular weight of specie ξ, and T_g is the gas temperature.

The average viscous stress tensor is approximated by a form similar to its microscopic counterpart $\overline{\boldsymbol{\tau}}_g = 2\mu_g \mathbf{S}_g$, where $\mathbf{S}_g$ denotes the strain rate tensor: $\mathbf{S}_g = (\nabla\widetilde{\mathbf{u}}_g + \nabla\widetilde{\mathbf{u}}_g^T)/2 - (\nabla \cdot \widetilde{\mathbf{u}}_g)/3$ and μ_g is the gas viscosity. The average specie flux $\bar{\mathbf{j}}_\xi$ is written as a simple gradient diffusion (Fickian) relation, neglecting multicomponent aspects:

$$\bar{\mathbf{j}}_\xi = -\overline{\rho}_g D_\xi \nabla \widetilde{Y}_\xi, \tag{13}$$

where D_ξ is the mass diffusion coefficient. Similarly, the average molecular heat flux $\overline{\mathbf{q}}_g$ is modeled in analogy with its molecular counterpart (Bird, 1960)

$$\overline{\mathbf{q}}_g = -\lambda_g \nabla \widetilde{T}_g - \sum_{\xi} h_\xi \bar{\mathbf{j}}_\xi \tag{14}$$

with λ_g denoting the heat conductivity coefficient, and where the second term represents the effect of species interdiffusion. Following Drew (1983), the momentum transfer term may be decomposed into two contributions:

$$\mathbf{M}_g = -p_g^i \nabla \alpha_g + \mathbf{M}'_g \tag{15}$$

where we have introduced the average interfacial gas pressure, p_g^i. The first term in eq. 15 accounts for the buoyant force while the second incorporates such forces as gas-particle drag, etc. The momentum equation is then

$$\frac{\partial \alpha_g \overline{\rho}_g \widetilde{\mathbf{u}}_g}{\partial t} + \nabla \cdot \alpha_g \overline{\rho}_g \widetilde{\mathbf{u}}_g \widetilde{\mathbf{u}}_g = -\alpha_g \nabla \overline{p}_g + \nabla \cdot [\alpha_g \overline{\boldsymbol{\tau}}_g + \boldsymbol{\Sigma}_g^{Re}] + \alpha_g \overline{\rho}_g \mathbf{f}_g + \mathbf{M}'_g + \Gamma_g \mathbf{u}_g^i \tag{16}$$

where the difference between the interfacial and the average gas pressure has been neglected, i.e. $p_g^i = \overline{p}_g$. Closure of the average transfer of mass, momentum and energy between the phases is derived below.

2.3 Particle phase transport equations

The transport equations are derived similarly to those for dense gases, using kinetic theory concepts. Important differences from classical kinetic theory are the inelasticity of collisions between macroscopic particles leading to dissipation, and the presence of an interstitial gas exerting drag on the particles, which leads to interaction terms in the averaged transport equations.

While a considerable literature exists on the development of equations of motion for multicomponent mixtures, most of it is restricted to the case where the temperatures and velocities of the species are nearly equal and evolve according to the dynamic equations of the mixture. This classical mixture theory (Chapman and Cowling, 1970) requires that $\Delta u/\Theta_c << 1$ (Δu being a characteristic relative velocity of the particle classes and Θ_c a characteristic rms velocity, related to a temperature in the molecular context). Furthermore, granular energy is assumed to be partitioned among the various particle classes according to their mass ratios (equipartition). The latter assumption is specifically inappropriate for granular flows due to the inelasticity of collisions. Therefore, here we derive separate dynamic equations for each of the particle classes, similar to that of Goldman and Sirovich (1967) for a dilute mixture of interacting species.

Let $f_i^{(1)}(\mathbf{x}, \mathbf{c}, Y_\xi, T, m, t)$ denote the single particle distribution function of particle class i such that $f_i^{(1)}$ is the probable number of particles of class i having their center of mass in the region $[\mathbf{x}, \mathbf{x} + d\mathbf{x}]$, a velocity in the region $[\mathbf{c}, \mathbf{c} + d\mathbf{c}]$, mass in the region $[m, m + dm]$, mass fractions in $[Y_\xi, Y_\xi + dY_\xi]$, and temperature in $[T, T + dT]$. The evolution of each of these distribution functions is governed by a set of Boltzmann equations (Simonin, 1996)

$$\frac{\partial f_i^{(1)}}{\partial t} + \frac{\partial}{\partial \mathbf{x}}[\mathbf{c}_i f_i^{(1)}] + \frac{\partial}{\partial \mathbf{c}_i}[\frac{\mathbf{F}_i}{m_i} f_i^{(1)}] + \frac{\partial}{\partial m_i}[\frac{dm_i}{dt} f_i^{(1)}] + \frac{\partial}{\partial T_i}[\frac{dT_i}{dt} f_i^{(1)}] + \sum_\xi \frac{\partial}{\partial Y_{i,\xi}}[\frac{dY_{i\xi}}{dt} f_i^{(1)}] = \sum_j J_{ij} \quad (17)$$

where $\mathbf{F}_i$ is the external force on the particle (gravity and particle drag). The right hand side represents the effect of collisions with particles of all classes.

The number density, n_i, of particle phase i follows by integration of the single-particle distribution function f_i over all of phase space

$$n_i(\mathbf{x}, t) = \int f_i d\mathbf{c} dY_\xi dT dm. \quad (18)$$

With the previously derived single-particle distribution, a particle average may be introduced as follows

$$\overline{\Psi}_i(\mathbf{x}, t) = \frac{1}{n_i} \int \Psi_i f_i d\mathcal{Z} \quad (19)$$

where $d\mathcal{Z}$ denotes the set of integration variables. The mass of the particles need not be a constant, therefore mass weighted averages are also introduced:

$$\widetilde{\Psi}_i(\mathbf{x}, t) = \frac{1}{\alpha_i \overline{\rho}_i} \int m_i \Psi_i f_i d\mathcal{Z} \quad (20)$$

where

$$\alpha_i \overline{\rho}_i = n_i \overline{m}_i = \int m_i f_i d\mathcal{Z}. \quad (21)$$

This definition of the mass-weighted particle average is completely comparable to that used for the carrier phase and leads to more convenient forms of the moment equations derived later. In the above expression, α_i denotes the local phase fraction of class i (where pores are excluded) and $\overline{\rho}_i$ its corresponding average particle density. We also introduce equivalent definitions for $\widehat{\alpha}_i$ and $\widehat{\rho}_i$ where the pores of the particles are counted as volume belonging to the particle. Note that $\alpha_i \overline{\rho}_i = \widehat{\alpha}_i \widehat{\rho}_i$. Mass weighted averages will also be denoted by brackets, i.e. $< \Psi >_i = \widetilde{\Psi}_i$ in the derivation below. Using the above definitions we define the average velocity $\mathbf{u}_i =< \mathbf{c}_i >$, the fluctuation velocity component, $\mathbf{C}_i = \mathbf{c}_i - \mathbf{u}_i$, and the granular temperature, $\Theta_i = \frac{1}{3} < C^2 >$. The solidity, $\eta = 1 - \epsilon$, where ϵ is the porosity of a particle, is defined as the ratio of the volume displaced by the particle and the volume displaced by the particle if its pores had been closed. The solidity is then easily shown to equal

$$\eta_i = \frac{m_i}{V_i} \sum \frac{Y_\xi}{\rho_\xi}. \quad (22)$$

In the present case of biomass pyrolysis, we assume that the particle diameter stays constant throughout the pyrolysis, and that the porosity of the particle simply increases in time (Miller and Bellan, 1997). This assumption is correct when the particle does not break or erodes.

The moment equations are derived by multiplying the Boltzmann equation by a variable $m\Psi$ and integrating over phase space. The general transport equation obtained is

$$\begin{aligned}\frac{\partial\alpha_i\bar{\rho}_i\widetilde{\Psi}_i}{\partial t}+\nabla\cdot(\alpha_i\bar{\rho}_i &< \mathbf{c}_i\Psi_i >) = \sum_{k=A,B} C_{ik}(m_i\Psi_i) + \\ \alpha_i\bar{\rho}_i &< \frac{\mathbf{F}_i}{m_i}\frac{\partial\Psi_i}{\partial\mathbf{c}_i} > +\alpha_i\bar{\rho}_i < \frac{dT_i}{dt}\frac{\partial\Psi_i}{\partial T_i} > + \\ \alpha_i\bar{\rho}_i\sum_{\xi} &< \frac{dy_{i\xi}}{dt}\frac{\partial\Psi_i}{\partial y_{i\xi}} > +\alpha_i\bar{\rho}_i < \frac{dm_i}{dt}[\frac{\partial\Psi_i}{\partial m_i}+\frac{\Psi_i}{m_i}] >\end{aligned} \tag{23}$$

where $C_i(m_i\Psi_i)$ is the mean collisional rate of change of particle property Ψ_i. It represents an integral over all possible (binary) collisions of the change in $m_i\Psi_i$ multiplied by the probability that such a collision occurs. Jenkins and Mancini (1987, 1989) show that this integral can be written as the sum of a source-like contribution and a flux term, representing transport by collisions:

$$C_{ik}(m_i\Psi_i) = \chi_{ik}(m_i\Psi_i) - \nabla\cdot\theta_{ik}(m_i\Psi_i) \tag{24}$$

The precise forms of these integrals is given in Appendix A where an outline is given on a method for calculating these collision integrals.

2.3.1 Collision dynamics

As in kinetic theory, it is assumed that only binary collisions occur, i.e. collisions among multiple particles are neglected. Although at high solids concentrations this assumption is questionable (especially when the particle size ratio is large), it is the only mathematically tractable approach (even in the simpler, molecular theory; see Chapman and Cowling, 1970).

As in Jenkins and Mancini (1987), we consider two particle classes, A and B, although more classes may be added without changing the formalism. These particles are assumed perfectly smooth and spherical. Their respective masses and diameters are m_A, m_B, σ_A, and σ_B. Consider a collision between particle 1 of class i and particle 2 of class k where i and k may be A or B. Furthermore, when considering collisions, primes will be used to denote a variable right after collision, a variable without a prime denoting a variable right before collision. Below we consider the conservation of momentum and energy (mass and species are trivial) during a collision between particle 1 and 2.

Momentum Assuming exclusively binary collisions and perfectly spherical and smooth particles, the relation between the velocities of the particles right before and after a collision of particle 1 of class i and particle 2 of class k is determined from the conservation of momentum and energy; see Chapman and Cowling (1970). Defining $\mathbf{g}$ as the relative velocity, $\mathbf{c}_1-\mathbf{c}_2$, we assume $\mathbf{g}$ before and after collision to be related as $(\mathbf{g}'\cdot\mathbf{k}) = -e_{ik}(\mathbf{g}\cdot\mathbf{k})$, where e_{ik} is the restitution coefficient, incorporating the effect of inelasticity on the collisions ($e_{ik}=1$ for perfectly elastic encounters). Further define the sum of the particle's masses $m_{ik}=m_i+m_k$ and the reduced mass $M_i=m_i/m_{ik}$. The center of mass velocity, $\mathbf{c}_m$, is constant during a collision and is found from

$$\mathbf{c}_m = M_k\mathbf{c}_2 + M_i\mathbf{c}_1 = M_k\mathbf{c}_2' + M_i\mathbf{c}_1'. \tag{25}$$

From these relations we derive,

$$\mathbf{c}_1' - \mathbf{c}_1 = -M_k(1+e_{ik})(\mathbf{g}\cdot\mathbf{k})\mathbf{k}. \tag{26}$$

In general, for any particle property $\Psi = \Psi(\mathbf{c})$, these relations may be used to calculate its rate of change $\Psi' - \Psi$ in a collision. In the above we have assumed that the collision is not abrasive, i.e. the mass the particles does not change during a contact.

Energy Sun and Chen (1988) presented a detailed analysis of the heat transfer between two colliding particles. Their theory is based on the analysis of the elastic deformation of the spheres as they contact, and the resulting heat conduction. Since detailed information may be found in the aforementioned reference, only the pertinent essentials are emphasized here. The spheres are termed with indices 1 and 2. If one defines the average radius, R, the average mass, m and the average elastic modulus, E as follows

$$R = \frac{R_1 R_2}{R_1 + R_2}; \; m = \frac{m_1 m_2}{m_1 + m_2}; \; E = \frac{4/3}{\frac{1-\nu_1^2}{E_1} + \frac{1-\nu_2^2}{E_2}} \tag{27}$$

where ν_i and E_i denotes the Poisson ratios and the Young moduli of the respective materials. The contact time is usually very small which implies that the temperature of the particle remains uniform except in a very small region around the contact area. For small Fourier numbers for both spheres, based on the total contact time, t_c and the contact area, A_c ($Fo = \pi a t_c / A_c$, with a the thermal diffusivity of the particle), the problem may be approximated by 2 contacting infinite plates. The heat exchange between the two particles in this simplified case is given by

$$\Delta E = \frac{5.36 (m/E)^{3/5} (Rg)^{7/10} (T_1 - T_2)}{(\rho c_p \lambda)_1^{-1/2} + (\rho c_p \lambda)_2^{-1/2}} \tag{28}$$

where g denotes the magnitude of $\mathbf{g}$ and the numerical constant is obtained from numerical integration. Sun and Chen (1988) further note that the small Fourier number approximation is valid if the velocity at which the particles collide is not too small ($\simeq$ 1 cm/s for sand).

2.3.2 Particle dynamics

The second component needed for the derivation of the moment equations is the rate of change of the particle properties along their trajectory.

Species mass fractions As outlined earlier, the mass conversion rates are linear in the mass of the particle itself. In general we may write

$$\frac{dm_{i,\xi}}{dt} = \frac{dmY_{i,\xi}}{dt} = mR_{i,\xi} \tag{29}$$

where $R_{i,\xi}$ represents the total rate, and may be the sum of several reactions involving the same component. The rate is linear in the mass fractions and exponential in the particle temperature (Arrhenius kinetics). From the previous equation one obtains the rate of change of $Y_{i,\xi}$

$$\frac{dY_{i,\xi}}{dt} = R_{i,\xi} - \frac{Y_{i,\xi}}{m_i} \frac{dm_i}{dt}. \tag{30}$$

Particle mass The rate of change of the particle mass is obtained by summing the individual species rates

$$\frac{dm_i}{dt} = \sum_{\xi} \frac{dm_{i,\xi}}{dt} = m_i \sum_{\xi} R_{i,\xi}. \tag{31}$$

In practice, only some reactions contribute to phase change.

Momentum The momentum equation of a single particle can be approximated as

$$m_i \frac{d\mathbf{c}_i}{dt} = \mathbf{F}_i = m_i \mathbf{f}_g - V_i \nabla \overleftrightarrow{p}_g + \frac{m_i}{\tau_{i,12}} (\overleftrightarrow{\mathbf{u}}_g - \mathbf{c}_i) \tag{32}$$

where the total force on the particle is due to the gravitational acceleration, $\mathbf{f}_g$, gas pressure gradient and gas-particle drag. V_i is the volume of the particle including the pores (i.e. $\pi d_i^3/6$) and $\tau_{i,12}$ represents the relaxation time scale of the particle. The $\overleftrightarrow{()}$ on the gas-phase variables denotes the evaluation of the variable at the location of the particle, as if the surrounding flow was undisturbed by its presence (Balzer et al.,1993). The gas-particle interaction time scale depends strongly on the flow regime; in the dilute regime it is derived from the drag coefficient, C_d, of a single particle in an infinite medium, empirically corrected for the presence of other surrounding particles by a function $f(\alpha_g) = \widehat{\alpha}_g^{-1.7}$ (e.g. Gidaspow, 1986) whereas in the dense regime the classical Ergun relation is used. To avoid discontinuous behavior, a weighted average of the two time scales is introduced

$$\frac{1}{\tau_{i,12}} = W \frac{3\rho_g C_d(Re_i)}{4\rho_i d_i} |\mathbf{c}_i - \overleftrightarrow{\mathbf{u}}_g| f(\widehat{\alpha}_g) + (1-W) \frac{\rho_g}{\rho_i} \left[(1-\widehat{\alpha}_g) \frac{150}{Re_i} + 1.75 \right] \frac{|\mathbf{c}_i - \overleftrightarrow{\mathbf{u}}_g|}{d_i} \tag{33}$$

where the present switch function, $W(\widehat{\alpha}_g) = \arctan(150(\widehat{\alpha}_g - 0.8))/\pi + 1/2$, gives a rapid transition from one regime to the other. d_i is the diameter of the particle and Re_i the Reynolds number based on the relative velocity with the gas, $Re_i = \widehat{\alpha}_g \rho_g |\mathbf{c}_i - \overleftrightarrow{\mathbf{u}}_g| d_i / \mu_g$. In the above expressions we have introduced $\widehat{\alpha}_g$ which represents the volume fraction of the gas-phase, not counting the pores of the particles. The single particle drag coefficient C_d is determined from the well-known correlation (Schiller and Nauman, 1935)

$$C_d = \frac{24}{Re_p} (1 + 0.15 Re^{0.687}). \tag{34}$$

Although not attempted in the present work due to the different range in Re_p, this correlation may be further improved by adding a correction which results from the effect of mass transfer, as done in the validated model of Miller et al. (1999).

Energy The rate of change of the particle's internal energy is due to heat exchange with the surrounding gas resulting from convection and diffusion, loss of vapor components to the gaseous phase carrying a specific enthalpy, h_v, and expansion work performed against the gas phase

$$m_i \frac{dh_i}{dt} = Q_{r,i} + \frac{dm_i}{dt}(h_v - h_i) + \frac{m_i}{\rho_i} \frac{dp_g}{dt}. \tag{35}$$

Here, the particle's specific enthalpy, h_i, is defined as $h_i = \sum Y_{i,\xi} h_{i,\xi}$ and the average density of the particle is related to the 'true' densities of the individual solid species by $1/\rho_i = \sum Y_{i,\xi}/\rho_{i,\xi}$. The above equation, in fact defines the heat flux $Q_{r,i}$ (Young, 1995). It can also be written in terms of the particle temperature, T_i by using the thermodynamic differential for the specific enthalpy of a component:

$$dh_{i,\xi} = C_{p,i,\xi} dT_i + \frac{dp_g}{\rho_{i,\xi}} \tag{36}$$

where the pressure inside the particle has been equated to the gas pressure outside the particle. Using this relation in (35) leads to the expected result

$$(mC_p)_i \frac{dT_i}{dt} = Q_{r,i} + \sum \frac{dm_{i,\xi}}{dt}(h_v - h_\xi) \tag{37}$$

where the effect of pressure has cancelled, as it should. The second term on the right hand side is exactly equal to the total heat of reaction for the particle.

The combined effect of convective and conductive heat transfer can be written in terms of an appropriate Nusselt relation

$$Q_{r,i} = -\lambda_g \pi d_i Nu_i (T_i - \overleftrightarrow{T}_g) \tag{38}$$

where Nu_i depends on the Reynolds number of the particle and on the Prandtl number, Pr_g, of the carrier gas. In obtaining relevant Nusselt relations for this situation, it is assumed that the particle temperature is uniform, i.e. the resistance to heat transfer is mainly in the gas-phase. This assumption is consistent with those used to actually derive the continuum theory, as the state variables of the particles include their mean temperature only, i.e. no information on the internal temperature distribution is available. Implicitly, the Biot numbers are assumed small ($Bi = hd_i/\lambda_i$, where h is the gas-particle heat transfer coefficient). In the present case, the Nusselt number is taken as the single particle Nusselt relation, Nu_i^0, multiplied by a correction factor, F_b, accounting for the effect of mass transfer on the heat transfer rate, i.e.

$$Nu = Nu^0 F_b(Re, Pr_g). \tag{39}$$

The formulation used here for the blowing factor is that taken from Miller et al. (1999) and was also given by Gyarmathy (1982) where the factor depends on the 'blowing Reynolds number', $Re_b = \overset{\bullet}{m} / \pi d_i \mu_g$,

$$\begin{aligned} F_b &= \frac{X}{e^X - 1}; \\ X &= \frac{Pr_g Re_b}{2}. \end{aligned} \tag{40}$$

For Nu^0, we use the standard Ranz correlation

$$Nu^0 = 2 + 0.66 Re^{1/2} Pr^{1/3}. \tag{41}$$

There does not appear to be much information on the dependence of Nu^0 on α_g for cases where the particle number density is high, such as in the packed region. A correlation, based on experimental observations, proposed by Gunn (1978) for the porosity range of 0.35 to 1 is

$$Nu^0 = (5\alpha_g^2 - 10\alpha_g + 7)(1 + 0.7Re^{0.2}Pr^{1/3}) + (1.2\alpha_g^2 - 2.4\alpha_g + 1.33)Re^{0.7}Pr^{1/3} \tag{42}$$

In the limit of $\alpha_g \rightarrow 1$, this relation reduces to

$$Nu^0 = (2 + 1.4Re^{0.2}Pr^{1/3}) + 0.13Re^{0.7}Pr^{1/3} \tag{43}$$

which clearly illustrates its discrepancy with the commonly accepted Ranz relation. Furthermore, the values of the coefficients in the Gunn relation are not strong functions of the volume fraction: for α_g between 0.4 and 1, $5\alpha_g^2 - 10\alpha_g + 7$ varies between 3.8 and 2 while $1.2\alpha_g^2 - 2.4\alpha_g + 1.33$ varies between 0.56 and 0.13. For these reasons, the single-sphere relation is adopted here. Heat transfer through radiation is neglected since the gas is considered transparent.

2.3.3 The moment equations

By making specific choices for the general variable Ψ in the transport theorem, specific moment equations are recovered.

Mass The mass conservation equations are recovered by taking $\Psi = 1$:

$$\frac{\partial(\alpha_i\overline{\rho}_i)}{\partial t} + \nabla\cdot(\alpha_i\overline{\rho}_i\mathbf{u}_i) = \Gamma_i \tag{44}$$

where the mass transfer $\Gamma_i = \alpha_i\overline{\rho_i} < \frac{1}{m_i}\frac{dm_i}{dt} >= \alpha_i\overline{\rho_i}\sum_\xi < R_{i,\xi} >$ can be coupled to the conversion rate of solid- to gas-phase reactions. For inert particles, this term is absent.

Momentum The momentum equations are generated using $\Psi = \mathbf{c}$

$$\begin{aligned}\frac{\partial(\alpha_i\overline{\rho}_i\mathbf{u}_i)}{\partial t} + \nabla\cdot(\alpha_i\overline{\rho}_i\mathbf{u}_i\mathbf{u}_i) &= \alpha_i\overline{\rho}_i < \frac{\mathbf{F}_i}{m_i} > + \alpha_i\overline{\rho}_i < \frac{dm_i}{dt}\frac{\mathbf{c}_i}{m_i} > \\ &\quad -\nabla\cdot\mathbf{\Sigma}_i + \sum_{k=A,B}\chi_{ik}(m_i\mathbf{C}_i)\end{aligned} \tag{45}$$

where $\mathbf{\Sigma}_i = \alpha_i\overline{\rho}_i < \mathbf{C}_i\mathbf{C}_i > + \sum_{k=A,B}\theta_{ik}(m_i\mathbf{C}_i)$. The first term on the right hand side of eq. **??** is the average force exerted on the particle by the surrounding gas; the second represents the effect of mass transfer. The effective stress tensor $\mathbf{\Sigma}_i$ consists of a kinetic part and a collisional part which incorporates both effects from collisions between particles of the same class and between unlike particles. The final term in the transport equation is a source term which is also composed of collisional contributions between like and unlike particles. However, as the total momentum of phase i is conserved in a collision between two particles of that phase, only unlike particle collisions contribute to this term. Note that an equivalent term does not appear in single-class formulations.

Species mass fractions Taking $\Psi = Y_\xi$ gives

$$\frac{\partial(\alpha_i\overline{\rho}_i\widetilde{Y}_{i\xi})}{\partial t} + \nabla\cdot(\alpha_i\overline{\rho}_i\mathbf{u}_i\widetilde{Y}_{i\xi}) = -\nabla\cdot(\alpha_i\overline{\rho}_i < \mathbf{C}_i Y'_{i\xi} >) + \Gamma_{i\xi}. \tag{46}$$

The first term on the right hand side denotes the turbulent transport of the mass fraction. The second term, $\Gamma_{i\xi} = \alpha_i\overline{\rho}_i < R_{i,\xi} >$ is the average mass source arising from reaction. Note that no collisional terms are present, as the mass fractions do not change during a collision.

Granular temperature Choosing $\Psi = 1/2C^2$

$$\begin{aligned}\frac{3}{2}\left[\frac{\partial(\alpha_i\overline{\rho}_i\Theta_i)}{\partial t} + \nabla\cdot(\alpha_i\overline{\rho}_i\mathbf{u}_i\Theta_i)\right] &= -\mathbf{\Sigma}_i : \nabla\mathbf{u}_i - \nabla\cdot\mathbf{q}_i \\ +\gamma_i + \alpha_i\overline{\rho}_i &< \frac{dm_i}{dt}\frac{1/2C_i^2}{m_i} > + \alpha_i\overline{\rho}_i < \frac{\mathbf{F}_i}{m_i}\cdot\mathbf{C}_i >,\end{aligned} \tag{47}$$

where $\Theta_i = 1/3 < C_i^2 >$ is the 'granular temperature'. The first term on the right hand side of eq. 47 is the production of fluctuation kinetic energy due to shearing of the solid phase. $\mathbf{q}_i = \alpha_i\overline{\rho}_i < 1/2C_i^2\mathbf{C} > + \sum_{k=A,B}\theta_{ik}(1/2m_iC_i^2)$ is the average 'heat flux' both due to velocity fluctuations and through collisions. The source term, $\gamma_i = \sum_k\chi_{ik}(\frac{1}{2}m_iC_i^2)$, represents the effects of energy redistribution among particle classes and the dissipative effect of inelastic collisions. Similar to the momentum equation, the source term is composed of a sum over both particle classes. Here, however, due to the inelasticity of collisions, all collision types contribute. The effect of mass transfer is contained in the next to the last term of eq. 47. The final term, which may be either a source or sink, represents the coupling with the surrounding gas phase.

Energy Choosing $\Psi = h$, one obtains

$$\begin{aligned}\frac{\partial(\alpha_i \overline{\rho}_i \widetilde{h}_i)}{\partial t} + \nabla \cdot (\alpha_i \overline{\rho}_i \mathbf{u}_i \widetilde{h}_i) &= \alpha_i \overline{\rho}_i < \frac{Q_{r,i}}{m_i} > + \alpha_i \overline{\rho}_i < \frac{1}{\rho_i} \frac{dp_g}{dt} > + \alpha_i \overline{\rho}_i < \frac{dm_i}{dt} \frac{h_v}{m_i} > \\ &\quad - \nabla \cdot \alpha_i \overline{\rho}_i < \mathbf{C}_i h_i' > \end{aligned} \tag{48}$$

Here, the terms on the right hand side denote the mean heat transfer with the surrounding gas, the effect of mean enthalpy carried by the vapors exiting the porous particle, and the 'turbulent' flux. The collision terms are negligible, as shown by the analysis given in Appendix B.

2.4 Closure

The above model describes a particle mixture in a gaseous carrier using conservation equations for mass, momentum energy and granular temperature of each solid class. These multiple-class equations describe the independent accelerations of the species, as well as momentum and energy exchange between solids classes. Moreover, these transport equations are valid even when Δu is of the same order as Θ_c, and when the granular temperatures do not obey the equipartition law. The above system of equations contains several correlations, and is therefore unclosed. These correlations are of several types: (i) collisional contributions to both transport and source terms, (ii) exchange terms between gas and solid, (iii) in-phase transport terms and transport properties.

In principle, the single particle distribution functions are solutions of the Boltzmann equations (17), however, they are difficult to obtain in situations when the phase space includes many variables (mass fractions, temperature, etc.). Therefore, it is assumed that the velocity distribution function for solution of the hydrodynamic problem can be obtained without incorporating the explicit effect of the thermochemistry. The hydrodynamic problem is then basically decoupled from the thermochemistry as far as the velocity distribution is concerned, and the velocity distributions may be obtained by similar techniques as are used in non-reactive flow, taking into account the mean evolution of, for instance, the particle mass. The single particle distribution function is then considered to be

$$f_i^{(1)}(\mathbf{x}, \mathbf{c}_i, Y_{\xi,i}, m_i, T_i, t) = f_i^{(1)*}(\mathbf{x}, \mathbf{c}_i, t)\delta(m_i - \overline{m}_i)\delta(T_i - \widetilde{T}_i)\sum_{\xi} \delta(Y_{\xi,i} - \widetilde{Y}_{\xi,i}) \tag{49}$$

where $f_i^{(1)*}$ is commonly called the velocity distribution, excluding the effect of particle mass, particle temperature, and species concentrations. For convenience, the asterisk is omitted on subsequent use of the velocity distribution.

2.4.1 Collisional and kinetic contributions

Additional to decoupling thermochemistry from hydrodynamics, a further simplification is made herein. Instead of using a distribution computed from the Boltzmann equations (excluding the effects of the thermochemistry), a Maxwellian distribution is assumed, i.e. the lowest order approximation to the Boltzmann equation in the absence of dissipative effects

$$f_i^{(1)}(\mathbf{x}, \mathbf{c}_i, t) = \frac{n_i}{(2\pi\Theta_i)^{3/2}} \exp[\frac{-(\mathbf{c}_i - \mathbf{u}_i)^2}{2\Theta_i}]. \tag{50}$$

This is a good approximation when the flow has small spatial gradients, the collisions are nearly elastic and the particles are sufficiently heavy (i.e. the time between collisions is much smaller than the particle relaxation time; the particle-fluid correlation is small). The integrals require specification of the radial distribution function at contact, $h_{ik}(\mathbf{r})$ (see Appendix A), accounting for the effects of excluded area and particle shielding on the spatial distribution of colliding pairs. The form of the radial distribution function is taken from Jenkins and Mancini (1987), slightly adjusted to prevent overpacking of the solids

$$h_{ik} = \frac{1}{1-\widehat{\alpha}/\alpha_0} + 6\frac{\sigma_i\sigma_k}{\sigma_i+\sigma_k}\frac{\xi}{(1-\widehat{\alpha}/\alpha_0)^2} + 8\left(\frac{\sigma_i\sigma_k}{\sigma_i+\sigma_k}\right)^2\frac{\xi}{(1-\widehat{\alpha}/\alpha_0)^2}. \tag{51}$$

Here $\widehat{\alpha}$ denotes the total particle volume fraction, accounting for the porosity inside the particles, and $\xi = 2\pi/3\sum n_i\sigma_i^2$ where σ_i denotes the radius of a particle of class i. The present paper is targeted towards dense systems where the drift between particle classes is small. In our context, using distributions where each particle class has its own mean velocity introduces unnecessary complexity (also see Appendix A). Therefore, the collision integrals are approximated by assuming that the relative velocity $\Delta\mathbf{u}_{ik} = \mathbf{u}_i - \mathbf{u}_k$, is small compared to the square root of the sum of the granular temperatures, $(\Theta_i + \Theta_k)^{1/2}$. This significantly simplifies the calculation of the required integrals, and furthermore should not affect the applicability of the equations for our purposes; this assumption is also the basis of the classic Enskog expansion where in addition the granular temperatures are assumed equilibrated. Here, the effects of having different granular temperatures for each particle class is, however, fully retained, which is important in these dissipative systems, leading to deviations from equipartition.

Manger (1996), assumed a distribution identical to ours in order to obtain closure for a binary mixture. In the work of Kumaran and Koch (1993a,b) the authors considered a slightly more general velocity distribution, i.e. an anisotropic Gaussian, where a distinction is made between the direction of gravity and the direction perpendicular to it. Although slightly more general, their work was restricted to homogeneous flows and is algebraically difficult to extend to inhomogeneous flows. Recently, Gourdel et al. (2000), also used Gaussians but they allowed for large drift between particle classes, leading to a theory suitable for the complete range of particle densities, i.e. from dilute to densely packed. Their work, however, was also restricted to homogeneous flows.

Using the above distributions and neglecting products of the spatial gradients, products of $(1-e_{ik})$ with spatial gradients, and products of $\Delta\mathbf{u}_{ik}$ with the spatial gradients, yields the following constitutive equations for $\boldsymbol{\phi}_i$, $\boldsymbol{\Sigma}_i$, $\mathbf{q}_i$, and γ_i. Some details on the computation of the integrals leading to the final result are listed in Appendix A

$$\begin{aligned}
\boldsymbol{\phi}_i &= \sum_k F_{ik}\left\{\frac{4}{3}\sqrt{2\pi}(\Theta_i+\Theta_k)^{1/2}(\mathbf{u}_k-\mathbf{u}_i) + \frac{\pi}{3}\sigma_{ik}(\Theta_i+\Theta_k)\nabla\ln\frac{n_i}{n_k}\right\} &\quad (52)\\
\boldsymbol{\Sigma}_i &= n_i m_i\Theta_i + \sum_k\left\{p_{ik}\mathbf{I} - \mu_i^{ik}[2\mathbf{S}_i + \frac{5}{3}\nabla\cdot\mathbf{u}_i] - \mu_i^{kk}[2\mathbf{S}_k + \frac{5}{3}\nabla\cdot\mathbf{u}_k]\right\} &\quad (53)\\
\mathbf{q}_i &= \sum_k\left\{\kappa_i^{ik}\nabla\Theta_i + \kappa_i^{kk}\nabla\Theta_k\right\} &\quad (54)\\
\gamma_i &= \sum_k -2\sqrt{2\pi}F_{ik}(\Theta_i+\Theta_k)^{1/2}\left\{2(M_i\Theta_i - M_k\Theta_k) + M_k(1-e_{ik})(\Theta_i+\Theta_k)\right\} &\quad (55)
\end{aligned}$$

where $F_{ik} = n_i n_k m_i M_k(1+e_{ik})h_{ik}\sigma_{ik}^2$. The indices on the viscosities and conductivities are arranged as follows, the subscript i indicates the relevance for class i, the first superscript labels the pertinent velocity gradient, and the k superscript denotes the dependence of the expressions on k. The pressure and transport coefficients are

$$\begin{aligned}
p_{ik} &= \frac{1}{3}\pi n_i n_k m_i M_k (1+e_{ik}) h_{ik} \sigma_{ik}^3 (\Theta_i + \Theta_k) && (56)\\
\mu_i^{ik} &= \frac{1}{15}\sqrt{2\pi} n_i n_k m_i M_k^2 (1+e_{ik}) h_{ik} \sigma_{ik}^4 (\Theta_i + \Theta_k)^{3/2}/\Theta_i && (57)\\
\mu_i^{kk} &= \frac{1}{15}\sqrt{2\pi} n_i n_k m_k M_i^2 (1+e_{ik}) h_{ik} \sigma_{ik}^4 (\Theta_i + \Theta_k)^{3/2}/\Theta_k && (58)\\
\kappa_i^{ik} &= \frac{1}{3}\sqrt{2\pi} n_i n_k m_i M_k (1+e_{ik}) h_{ik} \sigma_{ik}^4 (\Theta_i + \Theta_k)^{1/2} (M_k \Theta_k/\Theta_i) && (59)\\
\kappa_i^{kk} &= \frac{1}{3}\sqrt{2\pi} n_i n_k m_i M_k (1+e_{ik}) h_{ik} \sigma_{ik}^4 (\Theta_i + \Theta_k)^{1/2} (M_i \Theta_i/\Theta_k). && (60)
\end{aligned}$$

The terms in $\boldsymbol{\phi}_i$ represent solid-solid drag and ordinary diffusion, respectively (thermal diffusion has been neglected). The stress tensor depends on the shear rates of all solid classes where the shear viscosities arise entirely from collisions, not from streaming; this is a result of the Gaussian approximation. Similar remarks hold for the heat flux vector. Manger (1996) has presented similar closure relations for binary mixtures. For coding purposes, the shear rates of both phases are assumed equal (small drift) so that the actually used viscosity equals the sum of several contributions: $\mu_i = \sum_k \mu_i^{ik} + \mu_i^{kk}$. The source terms in the granular energy equations contain two terms: a temperature equilibrating and a dissipative term.

2.4.2 Exchange terms

A prerequisite for closing the formulation is the evaluation of exchange terms between each particle class and the carrier gas.

Mass and species The mass exchange terms in the mass and species equations are evaluated at the average temperature and mass fractions, i.e.

$$\Gamma_i = \alpha_i \bar{\rho}_i \sum_\xi \widetilde{R}_{i,\xi}^{s\to g} = \alpha_i \bar{\rho}_i \sum_\xi R_{i,\xi}(\{\widetilde{Y}\}, \widetilde{T}_i) \tag{61}$$

where $\{\widetilde{Y}\}$ denotes any combination of the set of species mass fractions and where only solid to gas reactions need to be considered. Although this procedure neglects correlations between particle temperature and the mass fractions, these approximations are not too strict since the reaction rates are first order with respect to the species, and therefore do not exhibit the stronger nonlinearity normally associated with second or higher order reaction rates. For consistency between the solids and gas phase we require

$$\Gamma_g = -\sum_i \Gamma_i. \tag{62}$$

A similar approach is followed for the reactive source terms in the individual species mass fraction equations for both carrier gas and the solid classes. Thus, these are evaluated at the mean temperature and mass fractions

$$\alpha\bar{\rho}\widetilde{R}_\xi = \alpha\bar{\rho}R_\xi(\{\widetilde{Y}\}, \widetilde{T}). \tag{63}$$

Interfacial species transfer occurs only for the tar and gas species. The combined terms $H_{g\xi} + \Gamma_g Y_{g\xi}^i$ form a mass source for the species equations originating from the appropriate solid to gas phase reactions (see section 2.1 for the kinetics) which is calculated from the mean particle temperature and mean solid phase mass fractions

$$H_{g\xi} + \Gamma_g Y^i_{g\xi} = \sum_i \alpha_i \overline{\rho}_i R_{i,\xi}(\{\widetilde{Y}\}, \widetilde{T}_i). \tag{64}$$

Enthalpy We first remark that the enthalpy equations of the gas and solid phases may be rewritten in non-conservative form:

$$\begin{aligned}(\alpha\overline{\rho}C_p)_g \frac{D\widetilde{T}_g}{Dt} &= -\nabla \cdot (\alpha\mathbf{q})_g + F_g + \Gamma_g(h^i_g - \widetilde{h}_g) && (65)\\ (\alpha_i\overline{\rho}C_p)_i \frac{D\widetilde{T}_i}{Dt} &= \alpha_i\overline{\rho}_i < \frac{Q_{r,i}}{m_i} > +\alpha_i\overline{\rho}_i < \frac{dm_i}{dt}\frac{(h_v - \widetilde{h}_i)}{m_i} > -\nabla \cdot \alpha_i\overline{\rho}_i < \mathbf{C}_i h'_i > && (66)\end{aligned}$$

where the gas pressure derivative in the solid equations has vanished; alternatively, one may start with the particle equation in terms of the particle temperature, eq. 37. The last term in the solids equation is the average reaction heat of all particle reactions (including solid to gas conversions). The energy equation contains the interaction term $\alpha_i\rho_i < Q_{r,i} >$ that accounts for the gas-particle heat transfer. The following closure is provided for this term

$$\alpha_i\rho_i < \frac{Q_{r,i}}{m_i} >= -\frac{6\widehat{\alpha}_i\lambda_g}{d_i^2} < Nu_i > (\widetilde{T}_i - \widetilde{T}_g), \tag{67}$$

where the average Nusselt number is calculated from the mean slip velocity, etc. For low turbulence intensity of the gas and solids (compared to the average slip velocity), this is an accurate approximation. Although Louge et al. (1993) have incorporated the effect of particle velocity fluctuations on the Nusselt number, considering the complexity of the present problem including porous particles, heat transfer and chemical reactions, such an approach has not been pursued here. The enthalpy flux associated with the vapor exiting the particle (tar and gas), $\sum_i \alpha_i\overline{\rho}_i < \frac{dm_i}{dt}\frac{h_v}{m_i} >$, requires knowledge of the specific enthalpies of the respective components. Such detailed properties are unknown in the present case where many components are lumped together into pseudo-components referred to as gas and tar. This enthalpy flux is only needed for the gas-phase, as the vapor enthalpy term is part of the total heat of reaction for the solids. To obtain closure, the differences in the formation enthalpies between the gas and the exiting vapors are neglected. We then obtain final closure of the gas-phase equation

$$\begin{aligned}F_g + \Gamma_g(h^i_g - \widetilde{h}_g) &= \sum_i \frac{6\widehat{\alpha}_i\lambda_g}{d_i^2} < Nu >_i (\widetilde{T}_i - \widetilde{T}_g) + && (68)\\ &\sum_i \Gamma^{s\rightarrow g}_{tar}(C^{tar}_p\widetilde{T}_b - C_{p,g}\widetilde{T}_g) + \Gamma^{s\rightarrow g}_{gas}(C^{gas}_p\widetilde{T}_i - C_{p,g}\widetilde{T}_g),\end{aligned}$$

where we have further assumed that the vapor products are leaving the particle at its mean temperature, and where $\Gamma^{s\rightarrow g}_{tar}$, and $\Gamma^{s\rightarrow g}_{gas}$ denote the averaged mass transfer rates of respectively, tar and gas.

Momentum The mass transfer related term is modeled using a mean value approximation, i.e.

$$\Gamma_g\mathbf{u}^i_g = \sum_i < \frac{dm_i}{dt}\frac{\mathbf{c}_i}{m_i} >= \sum_i \Gamma_i\widetilde{\mathbf{u}}_i. \tag{69}$$

Hence, the average interfacial gas velocity is approximated by the mean velocity of the particle class responsible for the mass transfer. The interaction term in the momentum equation may be expanded to

$$\alpha_i\overline{\rho}_i < \frac{\mathbf{F}_i}{m_i} >= \alpha_i\overline{\rho}_i[\mathbf{f}_g - < \frac{V_p}{m_i}\nabla\overleftrightarrow{p}_g > - < \frac{1}{\tau_{12}}(\mathbf{w}_i - \overleftrightarrow{\mathbf{u}}_g) >]. \tag{70}$$

The pressure gradient term is closed in terms of the mean gas pressure gradient:

$$-\alpha_i\overline{\rho}_i < \frac{V_p}{m_i}\nabla\overleftrightarrow{p}_g > \approx -\widehat{\alpha}_i\nabla\overline{p}_g. \tag{71}$$

Similarly, for the drag force related term:

$$-\alpha_i\overline{\rho}_i < \frac{1}{\tau_{12}}(\mathbf{c}_i - \overleftrightarrow{\mathbf{u}}_g) > \approx -\frac{\alpha_i\overline{\rho}_i}{\tau_{12}}(\mathbf{u}_i - < \overleftrightarrow{\mathbf{u}}_g >_i), \tag{72}$$

where fluctuations in the particle relaxation time are neglected. The particle average of the locally undisturbed velocity is set equal to the phase averaged velocity: $< \overleftrightarrow{\mathbf{u}}_g > \approx \widetilde{\mathbf{u}}_g$. For consistency between the gas and solids equations, $\mathbf{M}'_g = \sum_i \frac{\alpha_i\rho_i}{\tau_{i,12}}(\mathbf{u}_i - \widetilde{\mathbf{u}}_g)$.

Granular energy Two terms require closure, the mass transfer related correlation and the term related to the presence of an interstitial gas. The transfer term is closed assuming that fluctuations in the granular temperature are negligible, i.e.

$$< \frac{dm_i}{dt}\frac{1/2C_i^2}{m_i} >= \Gamma_i\Theta_i. \tag{73}$$

The interaction term with the gas phase can be expanded as

$$\alpha_i\overline{\rho}_i < \frac{\mathbf{F}_i}{m_i}\cdot\mathbf{C}'_i >= \frac{\alpha_i\overline{\rho}_i}{\tau_{12}}(< \mathbf{C}'_i\cdot\mathbf{u}''_g >_i - < \mathbf{C}'_i\cdot\mathbf{C}'_i >_i) \tag{74}$$

where gas pressure gradient fluctuations have been neglected and we have decomposed the undisturbed gas velocity in a mean value at the particle location and a fluctuation $\overleftrightarrow{\mathbf{u}}_g =< \overleftrightarrow{\mathbf{u}}_g >_i + \mathbf{u}''_g$. For fairly large particles, having large particle fluid interaction time compared to the time between collisions, the term in (74) may be neglected (dry granular mixture).

2.4.3 In-phase transport fluxes and evaluation of transport properties

Many of the transport closure used for the gas-phase have already been outlined in the section on gas-phase averaging. Here we focus on the solid-phase closure. The in-phase transport fluxes for the solids classes comprise the correlations between the velocity of the respective class and a variable, not explicitly considered in the distribution function, i.e. the species mass fractions, $Y_{i\xi}$, the particle mass, m or the temperature T. These transport fluxes arise from the self-diffusive transport of the respective property, carried by the particles. In analogy with the work of Louge et al. (1993), these 'turbulent' fluxes are modeled using a self-diffusive coefficient, D_{ii}, derived from the Gaussian velocity distribution

$$-\nabla\cdot(\alpha_i\overline{\rho}_i \quad < \quad \mathbf{C}_i Y'_{i\xi} >) = \nabla\cdot(\alpha_i\overline{\rho}_i D_{ii}\nabla\widetilde{Y}_{i\xi}) \tag{75}$$

$$-\nabla\cdot(\alpha_i\overline{\rho}_i \quad < \quad \mathbf{C}_i h'_{i\xi} >) = \nabla\cdot(\alpha_i\overline{\rho}_i C_{p,i} D_{ii}\nabla\widetilde{T}_i) \tag{76}$$

$$-\nabla\cdot(\alpha_i\overline{\rho}_i \quad < \quad \mathbf{C}_i m'_i >) = \nabla\cdot(\alpha_i\overline{\rho}_i D_{ii}\nabla\overline{m}_i) \tag{77}$$

The derivation of D_{ii} is detailed in Appendix C and follows the recent work of Hsiau (2000).

Transport properties are required for such parameters as the specific heats (both gas and solids) and thermal conductivities (gas only). These are calculated from a mass-weighted average of the individual species properties. Considering ϕ to be one such general property, its average is then computed from $\overline{\phi} = \sum_\xi Y_\xi \phi_\xi$. An exception to this procedure is in the calculation of the average particle density, $1/\overline{\rho}_i = \sum_\xi Y_{i,\xi} \rho_\xi$.

2.4.4 Transport equations for the mean particle mass and solidity

The transport theorem, used for the particle mass, gives a transport equations for $\widetilde{m}_i$, not $\overline{m}_i$. The approach used here is to equate the mass-weighted average to the non-weighted result; a procedure commonly practiced in work related to compressible single phase turbulence. The following transport equation then follows

$$\frac{\partial (\alpha \rho \overline{m})_i}{\partial t} + \nabla \cdot (\alpha \rho \mathbf{u} \overline{m})_i = \nabla \cdot \alpha_i \overline{\rho}_i D_{ii} \nabla \overline{m}_i - 2\Gamma_i \overline{m}_i \tag{78}$$

where turbulent diffusion has been included in a similar manner as in the energy and species equations and the factor 2 arises from the conservative form of the equation (both $\overline{m}_i$ and $(\alpha\rho)_i$ decrease due to mass transfer to the gas phase). The average solidity is then derived from the average particle mass as

$$\overline{\eta}_i = \frac{\overline{m}_i}{V_p} \sum_\xi \frac{\widetilde{Y}_\xi}{\rho_\xi}. \tag{79}$$

2.5 Frictional transfer

The constitutive equations derived above are restricted to the region where particles interact exclusively through slightly inelastic, short duration, collisions. However, as the volumetric fraction approaches the maximum packing volume fraction, α_0, particles will, increasingly, be in simultaneous contact with several neighbors and stresses will be transmitted at points of sustained sliding or rolling contact. This situation is very difficult to model at the microscopic level, leading to its neglect in many bubbling fluidized bed models. However, in certain regions where shear rates are very small, the granular temperature may be too small to support the solids phase. Hence, codes based on models neglecting friction require a 'numerical fix', generally restricting the value of the computed granular temperature (e.g. Boemer and Renz, 1997; Ma et al., 1993). To avoid this situation, we explicitly model the frictional regime, particularly since it was shown by Anderson and Jackson (1992) and Lathouwers and Bellan (2000a) that inclusion of the frictional regime is necessary for obtaining qualitatively correct results. The approach followed is similar to that used in Syamlal (1993), extended here for the case of multiple particle classes. The model proposed attains a simple relation between stresses and strains: $\mathbf{\Sigma}_i^f = -p_i^f \mathbf{I} + 2\mu_i^f \mathbf{S}_i$ for $\alpha > \alpha_{min}$ where α_{min} is the minimum solids fraction at which frictional transfer becomes influential. Experimental observations indicate that the frictional normal stress increases rapidly with bulk density and diverges as the maximum packing fraction, α_0, is approached (Savage and Sayed, 1984). A simple algebraic representation of this behavior is (cf. Anderson and Jackson, 1992)

$$p_i^f = \frac{\alpha_i \rho_i}{\sum \alpha_i \rho_i} Fr \frac{(\widehat{\alpha} - \alpha_{min})^p}{(\alpha_0 - \widehat{\alpha})^n} \tag{80}$$

where Fr is a material constant. The frictional viscosity, μ_i^f, is related to the frictional pressure and the angle of internal friction, ϕ, as $\mu_i^f = p_i^f \sin(\phi)/2\sqrt{I_2}$ where I_2 denotes the second invariant of the strain rate tensor. The following values for the parameters have been used in the present work: $p = 2$, $n = 5$, $Fr = 0.005$, $\alpha_{min} = 0.6$, $\alpha_0 = 0.64$, and $\phi = 25$ degrees, which are in general agreement with those of Anderson and Jackson (1992) and Johnson and Jackson (1987).

Following Johnson and Jackson (1987), the total stress is taken as the sum of the contributions from the separate mechanisms, each evaluated as though it acted alone: $\mathbf{\Sigma}^{tot} = \mathbf{\Sigma}^f + \mathbf{\Sigma}^c$. Here the superscript c indicates both collisional and kinetic contributions. However, in the production term of Eq. (47), the frictional terms are deleted, inherently assuming that the frictional work is directly converted to thermal internal energy.

3 Solution procedure

Spatial discretization of the governing equations is based on a finite volume technique using a staggered grid. All convective fluxes are approximated with a second-order accurate bounded TVD-scheme avoiding the excessive numerical diffusion associated with the first-order accurate upwind scheme which is still used today in many multiphase flow research codes (e.g. Mathiesen et al., 2000). The time discretization is based on a backward Euler scheme in combination with a pressure-correction technique. The momentum equations of all phases are solved in a coupled manner, though separately for each velocity direction. Compared with the well-known Partial Elimination Algorithm (PEA) the present approach is more general (see Lathouwers, 1999 for more details on full-field coupling and multiphase pressure correction algorithms). The species and energy equations constitute a strongly coupled, stiff system of equations. To avoid very large linear systems arising from (the necessarily) implicit discretization, a time splitting is used (Strang, 1968) for the combined species and energy system consisting of three steps: (i) performance of a half convection-diffusion timestep, (ii) time integration of the equations over a full timestep with only the reactive terms present, (iii) performance of another half convection-diffusion timestep. The advantage of this split scheme is that during steps (i) and (iii), the equations are decoupled into standard convection-diffusion systems which are easily handled, whereas in step (ii) there is no spatial coupling. The stiff integration in step (ii) is performed by using the well-known stiff integrator VODE (Hindmarsh et al., 1989). All sparse linear systems arising from the discretization of convection-diffusion systems are solved with preconditioned Krylov methods (CG for the pressure Poisson equation and GMRES for the other transport equations; see e.g. Barrett et al., 1994).

4 Results

The model has been applied to a variety of testcases in order to quantify its predictive capabilities. These are (i) the shearing of a homogeneous mixture, (ii) comparison of the particle pressure generated along the wall of a bubbling fluidized bed, (iii) the characteristic behavior of homogeneously fluidized beds, and (iv) biomass particle pyrolysis calculations for a fluidized bed reactor and comparison of obtained yield to experimental data. The first three sets of calculations do not involve reacting biomass; the temperature of the gas and particles is fixed at the same value ($T = 300K$) and is uniform in the reactor.

4.1 Homogeneously sheared mixture

Savage and Sayed (1984) have measured the normal and shear stresses developed by granular materials in a shear flow cell. The binary mixture consists of polystyrene beads (specific gravity 1.095) where $d_A = 0.55$ and $d_B = 1.68 mm$, respectively with a restitution coefficient of 0.8. The solids fractions for the small and large particles constitute 30 and 70 percent of the total bulk solids volume fraction.

For the case of simple shear, the model presented above becomes a set of ODE's which have to be supplemented with boundary conditions on the solid surfaces of the shear cell. However, as the distribution of solids in the shear cell is unknown and the boundary conditions uncertain, we assume the velocity gradient to be uniform and equal for both particle classes. The system simplifies to two coupled algebraic equations for Θ_A and Θ_B, stating that production equals dissipation for each size class: $-\Sigma_{i,xy}\frac{du}{dy} + \gamma_i = 0$. Frictional transfer has been excluded from the present model. The present analysis differs from that in Farell et al. (1986), since unequal granular temperatures are used here and a different radial distribution function is employed. Fig. 1 shows the comparisons of the present numerical solution of the set of equations and the experimental results for the mixture shear stress and the normal stress as function of the shear rate du/dy and of the bulk volume fraction. Also shown are predictions with a single particle model using a mean particle diameter of $1.34 mm$. Generally, for the lower solids fractions, both theories somewhat overpredict the stresses. At the highest bulk solids fraction, all stress components are, however, strongly underestimated which most likely indicates that the transfer of momentum becomes affected by friction, which was neglected in this specific case. The present, more general, binary model predictions are higher than the corresponding predictions in Farell et al. (1986), owing to the separate granular temperatures for each class. At these diameter ratios (≈ 3), the temperatures do not equilibrate completely, leading to higher stress levels. The differences with the experimental data at lower solids bulk fraction are attributed to the assumption of Gaussian distributions and to the form of the radial distribution function to which the results are highly sensitive.

4.2 Particle pressure along the wall of a bubbling fluidized bed

To validate the solids pressure model, a comparison was made with the experimental data of Campbell and Wang (1991) reporting measurements of the solids pressure magnitude in a bubbling bed consisting of a square channel ($1.22 \times 0.127 \times 0.127 m^3$), homogeneously fluidized with air. The bed is initially filled with glass beads ($d_p = 0.5 mm.; \rho = 2500 kg/m^3$), to a depth of 43 cm. As three dimensional calculations are very computationally intensive, the square channel was approximated by a flat two-dimensional geometry having a width equal to the size of the channel. Calculations were performed at three conditions, i.e. at superficial gas-velocities of 0.4, 0.6 and 0.8 m/s. The grid consists of 40×96 points. Fig. 2 shows vertical profiles of the computed time-averaged (over left and right wall) solids pressure (kinetic plus frictional) along the wall, together with the experimental data of Campbell and Wang (1991). Considering the geometric approximation, the agreement is reasonable, demonstrating an increase of solids pressure with height caused by fluctuating particle motion as induced by bubble growth, and a decrease to zero at greater heights where the solids fraction vanishes. Furthermore, the calculated profiles exhibit an increase in solids pressure as the superficial gas velocity is increased. Most of the solids pressure originates from the kinetic part, not from the frictional regime. The remaining discrepancies with the experimental data are attributed to (i) an insufficient period of averaging causing scatter, and (ii) the geometric approximations made by simulating a two dimensional geometry which may change the bubble dynamics. A similar comparison was presented recently in Boemer and Renz (1997), using a kinetic theory model, but excluding frictional stresses. Although the period of averaging was similar (9 sec), their results exhibit rather spiky profiles.

4.3 Behavior of homogeneously fluidized beds

The present study focuses on the global behavior of homogeneously fluidized beds, as these are to be used for the biomass pyrolysis. The fluidized bed studied is $0.68m$ wide, initially filled up to $0.4m$ with sand ($\rho_s = 2600kg/m^3, d_p = 0.5mm$) or with a sand-biomass mixture (2/3 sand 1/3 biomass volumetrically; biomass properties: $\rho_b = 700kg/m^3, d_p = 0.5mm$). All computations were performed on a 40×128 grid. To trigger bubbling, a disturbance was introduced in the initial volume fraction distribution.

The obtained fields are transient owing to hydrodynamic instabilities giving rise to spatial inhomogeneity. Fig. 3 shows a snapshot of the solids volume fraction and phase velocities at $t = 3$ s. Bubbles can be identified which form at the bottom of the bed and rise, growing through coalescence, in accordance with visual observations in the bubbly flow regime. Typical bubble shapes consist of spheres with an excluded wake at the bottom; also in accordance with experimental data (cf. Balzer et al., 1993). Time-averaged results (not shown) lead to a flow pattern with two symmetric circulation loops and a solid fraction distribution showing a reasonably uniform dense lower bed and a gradually more diluted upper region. The solids fraction is not homogeneous over the width of the bed, exhibiting higher values at the lower near-wall region, induced by the large scale circulation.

Fig. 4 shows the time-averaged solids volume fraction (computed from data along the centerline) in the lower part of the bed as function of the superficial gas velocity, compared to an experimental correlation from Johnsson et al. (1991). Also shown is an equilibrium solution obtained from a balance between gravity, gas-pressure gradient and gas-solid drag. The computed solids fraction agrees quite well with the experimental correlation although some scatter is present in the simulated data due to the restricted period of time averaging. It is also concluded that the average lower-bed solids concentration is well predicted by the assumption of steady homogeneous flow.

To investigate the differences between a binary and a monodisperse mixture, 2 computations are compared: i) using the present binary flow model with sand and biomass properties for the separate solids classes, and ii) using a monodisperse model with volume fraction weighted particle properties. Qualitatively, the simulations exhibit very similar behavior. One important difference is however the predicted solids distribution. The different properties of the particles cause the particle mixture to segregate. A quantitative measure of segregation may be defined as $S = (0.2\alpha_s - 0.4\alpha_b)/(0.2\alpha_s + 0.4\alpha_b)$, being zero if no segregation is present and 1 or -1 for complete segregation.

Fig 5. shows instantaneous distributions of the solids fractions and of the segregation parameter in the bed at $t = 6$ sec. Though initially the solids are perfectly mixed, already at this short time scale, segregation of the mixture is significant on a local scale, S mostly ranging between -0.2 and 0.2 (negative inside bubbles, carrying biomass to the top of the bed). The segregation can also be quantified by the y-coordinate of the centers of mass of the sand and biomass, which are shown in Fig 6 as a function of time. It is shown that already one or two seconds after startup, segregation is significant and tends to increase with time. Segregation was found to increase when the size of the biomass particles was decreased, due to a greater difference in terminal velocity. The monodisperse simulation is clearly unable to predict any of these features.

4.4 Biomass particle pyrolysis in a fluidized bed reactor

Among the pyrolysis reactor designs investigated for commercial production of condensable tars from biomass, the fluidized bed reactor is potentially efficient due to the high particle heating rates that can be achieved (Scott et al., 1999) and its excellent mixing properties, assuring a reasonably uniform product quality. A further interesting feature of this type of reactor is that char does not accumulate in the bed, but is rapidly elutriated with the gas flow instead, after which it may be filtered out, making the reactor very suitable for continuous operation.

The fluidized bed reactor contains a large amount of sand that is used as inert bed material which acts as heat capacitor for the biomass that is injected into the bed. Fluidization of the sand-biomass mixture is generally achieved by using either hot steam or nitrogen, some of which is also injected with the biomass, therefore preheating it. Once the particles enter the reactor, the temperature of the biomass rises rapidly and pyrolysis rates increase causing solid biomass species to be converted into tar and gas which are subsequently ejected from the particle, while char which is also formed in the process maintains the particle matrix. Biomass particle pyrolysis is an endothermic process and heat has to be supplied continuously by the surrounding gas, which in turn gets is heated by the sand. The gaseous reaction products are convected out of the reactor together with the fluidization gas to locations where it is subsequently cooled (quenched) to prevent product degredation.

Although the process has received considerable attention experimentally (Scott and Piskorz, 1982, 1984), currently there are no thorough theoretical analyses available, adressing simultaneously all physico-chemical processes in the reactor. Most of the work to date has focused on single-particle pyrolysis in a gas stream which requires *a priori* knowledge of ambient gas flow parameters, its temperature in particular (Di Felice et al., 1999).

Below, we present quantitative results from numerical simulations based on a detailed mathematical model, including a realistic chemistry model that is able to differentiate between various feedstock.

4.4.1 Detailed physico-chemical parameters of biomass pyrolysis

The kinetics scheme of the present biomass pyrolysis model was already given in section 2. The main advantage of the present kinetics scheme is the ability to differentiate between feedstock through knowledge of the initial mass composition with respect to the primary components, cellulose, hemicellulose and lignin. All of the reaction rates in the model, K_j, are considered irreversible, first order Arrhenius

$$K_j = A_j exp(-E_j/R^0T), \tag{81}$$

with A denoting the rate constant, and E the reaction's activation energy, are tabulated in Table 1 (cf. Miller and Bellan, 1997) and are dependent of the source component. Due to a lack of more detailed knowledge, the heats of reaction are taken as independent of the source component. The polymerization reaction K_1 has $\Delta h_1 = 0kJ/kg$, reaction K_2 is endothermic with $\Delta h_2 = 255kJ/kg$, and both the char formation and the secondary tar reactions are exothermic with $\Delta h_2 = -20kJ/kg$ and $\Delta h_2 = -42kJ/kg$. All other properties of gaseous and solid species are listed in Tables 2 and 3, respectively.

4.4.2 Simulation details

A sketch of the simulated geometry and the boundary conditions employed is given in Figure 7. The geometry has been chosen to resemble that used in experiments by Scott and Piskorz (1982, 1984), among others. Although the real fluidized bed is a cylindrical vessel, for computational simplicity, the present computational domain is approximated to be rectangular. Some care must therefore be taken in translating/comparing experimental data to simulations. The biomass is fed through an inlet section in one of the side walls, together with an amount of gas, which preheats the biomass during the feeding process. The center of feedpoint 1 is located 4.6 cm from the bottom of the bed and has a height (area) of 1.86 cm; feeder no 2 has the same height (area) and is located 12.1

cm from the bottom. In the present simulations, the temperature of the gas used for fluidization is equal to that fed through the biomass feed section (T_g); the inlet temperature of the biomass, however is assumed to vary (T_b) to investigate the effect of preheating. Note that, regardless of the biomass feed temperature, the biomass compositions used at the inlet correspond to those of biomass that has not pyrolyzed, i.e. it is assumed that the residence time in the feeder is short (no appreciable biomass conversion) while the effective heating of the particles is as efficient as required (by specifying the required temperature). To vary the cellulose/hemicellulose/lignin proportions of the feedstock, bagasse, olive husk, maple, and oak are used in the simulations. The initial biomass composition of these biomass types are given in Table 4. The diameter of the sand and biomass particles is assumed 0.5 mm, which is a common value in practical operation. The biomass particles are assumed to have an initial porosity of 0.7 (cf. Miller and Bellan, 1997). The biomass feed flux is ramped from 0 at t=0 to a value of 0.5 kg/m^2s at t=0.5 s, after which it is kept constant (when two feedpoints are used, the flow is equally split between feedpoints). A constant value of 1 kg/m^2s is specified for the gas flux through the feeder. The gas flow used for fluidization of the mixture is varied from 0.3 to 0.4 kg/m^2s and is uniform over the bottom of the domain. A summary of all simulations performed is listed in Table 5. Initial conditions correspond to a bed filled with sand only up to a height of 0.163 m at a volume fraction of 0.6 which corresponds to dense packing. To initiate bubbling of the bed, several disturbances in the volume fraction are inserted. The initial temperature of the sand and the gas in the domain is set equal to the inlet temperature of the fluidization gas. Hence, it is assumed that the fluidization gas has preheated the sand, even though initially the sand bed is stationary. This does not affect the calculation of product yield, as we are interested in the asymptotic (i.e. long time) behavior of the reactor; that is long after which a statistically steady flowfield has emerged. All computations have been performed on a 40 × 148 grid (x and z directions respectively). No-slip and free slip conditions are used at walls for the gas and solid, respectively. At the outlet, the pressure is prescribed as atmospheric while solids are inhibited to exit the domain (simulating a fine solids-filtering grid).

4.4.3 Results

Regardless of the local phenomena in the reactor, the true measure of the reactor efficiency for the tar production can be quantitatively determined by comparing the actual mass of tar exiting the reactor (Ω_{tar}) and the amount still present in its interior (M_{tar}) to the biomass feed flow (M_{feed}):

$$\Omega_{tar} = \int_0^t \int_{outlet} (\alpha_g \rho_g \mathbf{u}_g Y_{tar}) \cdot \mathbf{dA} dt' \tag{82}$$

$$M_{tar} = \int_{reactor} (\alpha_g \rho_g Y_{tar}) dV \tag{83}$$

$$M_{feed} = \int_0^t \int_{inlet} (\alpha_b \rho_b \mathbf{u}_b) \cdot \mathbf{dA} dt' \tag{84}$$

where the subscript b denotes biomass. With these definitions, two measures for reactor performance are the yield (η) and the differential reactor efficiency (DRE), ϑ, cf. Miller and Bellan (1998):

$$\eta_{tar}(t) = \frac{\Omega_{tar} + M_{tar}}{M_{feed}} \tag{85}$$

$$\vartheta_{tar}(t) = \frac{\Omega_{tar} + M_{tar}}{\sum_{\xi}(\Omega_{\xi} + M_{\xi})} \tag{86}$$

where the summation is over the species tar, gas and char. These measures quantify the relative efficiency of reactor tar production relative to the biomass feed flow, and the relative proportion of tar produced compared to gas and char. Similar definitions are used for the reactor performance with respect to gas and char production.

Qualitative behavior To investigate the qualitative behavior of the reactor, snapshots of several variables have been plotted at t=2.5 s, representative for Run No 4.

Figure 8 illustrates contours of the volume fractions of the sand and biomass. The sand contours are similar to those obtained for isothermal simulations, as expected. The volume fraction of the biomass is generally very small due to the short simulation time. The biomass is fairly evenly distributed over the dense part of the bed, illustrating the effectiveness for solid mixing in fluidized beds.

In Figure 9, the partial macroscopic densities ($=\alpha\rho Y$) of the relevant gas and solid species are plotted. Therein, biomass refers to the sum of both virgin and active solid components. Both tar and gas densities are high at the same location which is a region where the biomass temperature has increased enough to produce large quantities of both gaseous products. The inhomogeneities in the partial densities are a result of both the inhomogeneous reaction rates and transport processes in the reactor. The char is almost uniform throughout the dense bed owing to the effective solid mixing.

Figure 10 shows contours of the temperatures of the gas, sand, and biomass. Both the gas and sand temperature are almost uniform and equal to the inlet gas temperature (and more importantly, the initial sand temperature), i.e. 800 K. The biomass temperature, however, varies significantly throughout the reactor, showing a distinctive pattern of biomass entering at the specified feed temperature (400 K), flowing clockwise, while at the same time heating up.

In Figure 11, the y-coordinate of the center of mass of the sand and biomass are plotted as a function of time. It shows the particular transient structure due to the bubbling of the bed (both sand and biomass fluctuate in phase). In general, the biomass is situated higher up in the bed than is the sand. This is caused by two effects: (i) the biomass density is much smaller than that of the sand due to its high porosity, and (ii) the general motion of the biomass is directed upwards right after feeding due to bubbling, while on downward motion the particles have already partially pyrolysed, before reaching the bottom of the bed (an exception being formed by the unreactive char which remains). This particle segregation may be detrimental to tar production, indicating the need to optimize this yield as a functions of reactor and feedstock parameters.

Parametric study This parametric study is devoted to finding optimum conditions for maximizing tar yield as function of the relevant operating parameters. The parameters investigated include the temperature of the inlet gas, the feed temperature of the biomass, the fluidization velocity (or flux), the location of the feedpoint(s), and the type of feedstock used for pyrolysis.

Figures 12 and 13 show the yield and differential reactor efficiency with respect to tar production, respectively. The strong dpendence of both yield and DRE are noteworthy. Comparing the yield with the DRE, it can be concluded that the reactor efficiency is a more practical way of examining efficiency than is the yield which is, however, the quantity of ultimate industrial interest. Both figures indicate that the efficiency for tar production reaches a maximum at either 750 or 800 K; an extended simulation time is required to draw a stricter conclusion with respect to the optimum temperature. The abrupt decrease in tar DRE at small times corresponds to the large char DRE (see Fig. 17) resulting from the low biomass temperature. As the biomass temperature increases, so does the tar DRE concomitantly with the reduction in char DRE. The tar DRE is reduced by the large char DRE at small gas temperatures, and by the large gas DRE at high gas temperatures (see Fig. 15). Figures 14 and 15 show similar results for the gas production. The yield indicates a monotonic increase as temperature is increased, however, the gas DRE seems to be minimized for $T_g = 750K$, indicating that this is the most likely optimal temperature for maximizing tar yield. Similarly, for the production of char, Figures 16 and 17 show that the of char production increases with T_g, as pyrolysis is more vigorous. However, the char DRE decreases with increasing T_g, in agreement with the known hindrance of char production at larger reactor temperatures.

Figures 18 to 23 show the effects of variations in biomass feed temperature, fluidization gas flux, and the biomass injection point, respectively on the tar yield and the tar differential reactor efficiency. The results show that the changes in these parameters cause only minor variations in the tar yield. The results should be interpreted accounting for the assumption of no pyrolysis before entering the reactor and uniform particle temperature (kinetically controlled regime).

Finally, Figures 24 and 25 show the effect of employing different biomass types as feedstock. Bagasse returns the highest tar yield due to the largest proportion of cellulose and the smallest proportion of lignin present in this feed, however its DRE is lowest due to the largest gas DRE (not shown). Basically, the formed tar decomposes to gas before it can be collected. This points out to the higher than optimal fluidizing gas temperature for this case.

5 Conclusions

A comprehensive mathematical model has been derived which is capable of predicting the thermofluid dynamics of dense reacting gas-solid mixtures. The model is based on a multifluid description obtained from systematic averaging of the local instantaneous equations using the kinetic theory of granular flows in combination with rigid sphere interaction models explicitly accounting for collisional transfer. Multiple solid classes are considered to enable a differentiation in either physical properties or thermochemical behavior of various particle types, e.g. fuel vs inert particles. Separate transport equations are used for each particle class, allowing for the independent acceleration of the particles in each class and non-equilibrium processes leading to momentum and energy exchange between respective classes, and between particles and the carrier gas. The model avoids heuristic extensions from monodisperse results which are common in literature (Syamlal, 1993; Mathiesen et al., 2000). To illustrate this general gas-solid reacting model, simulations are conducted for biomass pyrolysis in a fluidized bed. In this specific case, a previously validated, chemistry model for biomass particle pyrolysis (7 solid species, 2 gaseous species), capable of differentiating between different feedstocks is coupled to the hydrodynamics formulation.

The model has been applied to a variety of test cases in order to quantify its predictive capabilities. Comparison of shear and normal stress component predictions in a simple shear flow of a binary mixture ignoring frictional transfer, reveal that for the lower bulk fractions, the stresses are somewhat overpredicted, whereas for the higher bulk fractions they are underpredicted. A comparison has also been made for the time-averaged particle pressure along the wall of a bubbling fluidized bed for different values of the superficial gas velocity. Predictions are generally in reasonable agreement with the available experimental data. Additionally, predictions have been presented for a homogeneously aerated bed, both with sand particles and with a sand-biomass mixture. For the monodisperse case, predictions of the solids volume fraction in the lower part of the bed have been compared to an experimental correlation and agreement is fairly good. Computations of a mixture of sand and biomass have shown that the qualitative behavior of the flow is not changed. The binary mixture model predicted a significant amount of segregation, even during the short timespan here investigated. Finally, the model has been applied to high temperature particle pyrolysis in a lab-scale fluidized bed reactor for which a parametric study has been performed. The major operating parameter, determining the tar yield is the temperature of the fluidization gas. Optimum yield was found for a fluidizing gas temperature of 750-800 K. Parametric variations in other process parameters, such as fluidization flux, biomass feed temperature, and feed position were found to be of relatively minor importance.

The results of this comparison further indicate that the model captures the key features of the pyrolysis process, and is general enough to be used for the optimization of reactor geometries and operating parameters, such as gas temperature, biomass injection procedures, etc. The model is presently used to optimize and scale up a biomass pyrolysis reactor for the National Renewable Energy Laboratory (NREL) (Lathouwers and Bellan, 2000b).

The present theory can be extended to more general situations. Two such obvious extensions are: (i) The consideration of gas phase turbulence, a model which has already been briefly outlined (Lathouwers and Bellan, 1999). (ii) The generalization of the single particle distribution function by seeking a solution to the Boltzmann equations that includes the effect of the surrounding gas on the velocity distribution function. This will lead to more accurate closure relations in the dilute region and would extend the applicability of the model to e.g. circulating beds. Both of these extensions can be made along the lines of Grad's theory (Grad, 1949; Jenkins and Richman, 1985; Peirano and Leckner, 1998), extended to a multiple-class granular mixture.

6 Acknowledgments

This research was conducted at the Jet Propulsion Laboratory (JPL) and sponsored by the U.S. Department of Energy (DOE), with Mr. Neil Rossmeisel (DOE Headquarters) and Mr. D. Hooker (DOE Golden Center) serving as contract monitors, under an agreement with the National Aeronautics and Space Administration. Computational resources were provided by the supercomputing facility at JPL.

7 Appendix A: Estimate of the ratio of heat transfer through direct particle contact to gas-particle heat transfer

The goal is here to estimate the relevant timescales associated with gas-particle and particle-particle heat transfer. To leading order, the averaged energy equation for particle class i is

$$(\alpha\rho C_p)_i \frac{dT_i}{dt} = \frac{6\widehat{\alpha}_i \lambda_g Nu_i}{d_p^2}\Delta T_{gp} + \sum_k \chi_{ik}(\Delta E) \tag{87}$$

with the notation of the main text. To simplify the analysis, we assume non-porous particles ($\widehat{\alpha}_i = \alpha_i$). The timescale for gas-particle heat-transfer is thus readily identified:

$$\tau_{gi} = \frac{\rho_i C_p d_i^2}{6\lambda_g Nu_i}. \tag{88}$$

The source integral for collisional transfer is

$$\chi_{ik}(\Delta E) = \sigma_{ik}^2 \int \Delta E(\mathbf{g}\cdot\mathbf{k}) h_{ik} f_i f_k d\mathbf{k} d\mathbf{c}_1 d\mathbf{c}_2 dT_1 dT_2 \tag{89}$$

where the expression for ΔE is given by eq. 28 and the integration over the particle masses has already been carried out. In reality, the particles are not perfectly spherical. The radius of curvature R (entering the expression for ΔE) therefore has a distribution associated with it. This does not affect the estimate of the collision integrals, especially since we are interested in order of magnitude estimates. The integrand depends on the relative velocity as well as on the temperature difference of the particles, and therefore consistent with the formulation of section 2.4.

$$f_i = \frac{n_i}{(2\pi\Theta_i)^{3/2}} \exp[-\frac{(\mathbf{c}_1 - \mathbf{u}_i)^2}{2\Theta_i}]\delta(T_1 - \widetilde{T}_i(r,t)). \tag{90}$$

Simple estimates of the time-scale do not require the calculation of the source integral; it is sufficient to simply estimate it as $\nu_c\overline{\Delta E}$, where the overbar denotes the average energy exchange. $\overline{\Delta E}$ is estimated using the expression for ΔE, (eq. 28) and ν_c is the collision frequency. The collision frequency in the low-drift limit is

$$\nu_c = \pi n_i n_k h_{ik} \sigma_{ik}^2 \sqrt{8\pi(\Theta_i + \Theta_k)} \tag{91}$$

where σ_{ik} is the mean diameter and h_{ik} denotes the radial distribution function at contact. The integral is then readily estimated as

$$\chi_{ik}(\Delta E) \simeq \nu_c \frac{5(m/E)^{3/5}(Rg)^{7/10}}{(\rho C_p\lambda)_i^{-1/2} + (\rho C_p\lambda)_k^{-1/2}} \Delta T_{ik} \simeq \nu_c \frac{5(m/E)^{3/5}(R)^{7/10}(\Theta_2+\Theta_3)^{7/20}}{(\rho C_p\lambda)_i^{-1/2} + (\rho C_p\lambda)_k^{-1/2}} \Delta T_{ik} \tag{92}$$

where we have approximated the relative velocity of the colliding particles as the square root of the sum of the granular temperatures. The timescale for particle-particle heat transfer is thus

$$\tau_{ik} = \frac{(\alpha\rho C_p)_i}{\pi n_i n_k h_{ik}\sigma_{ik}^2\sqrt{8\pi(\Theta_i+\Theta_k)}} \times \frac{(\rho c_p\lambda)_i^{-1/2} + (\rho c_p\lambda)_k^{-1/2}}{5(m/E)^{3/5}(R)^{7/10}(\Theta_i+\Theta_k)^{7/20}} \tag{93}$$

To estimate the two time-scales we consider the following representative parameters appropriate for the dense regime (phases i and k denoting sand and biomass, respectively)

$$\begin{aligned}
Nu_i &= 2-5 \\
\lambda_g &= 5.10^{-2}\ J/msK \text{ (Miller and Bellan, 1997)} \\
\lambda_i &= 0.1\ J/msK \text{ (CRC, 1992)} \\
\lambda_k &= 1\ J/msK \text{ (CRC, 1992)} \\
\alpha_i &= \alpha_k = 0.25 \\
d_i &= d_k = 10^{-3}\ m. \\
E_i &= 10^{10}\ Pa. \text{ (CRC, 1992)} \\
E_k &= 7.10^{10}\ Pa. \text{ (CRC, 1992)} \\
\nu_i &= \nu_k = 0.16 \text{ (CRC, 1992)} \\
\rho_i &= \rho_k = 1000\ kg/m^3. \\
C_{p,i} &= C_{p,k} = 1000\ J/kgK. \\
\Theta_i &= 10^{-8} - 10^{-2}\ m^2/s^2.
\end{aligned}$$

The gas-particle heat transfer time-scale is then

$$\tau_{gi} = \frac{\rho_i C_i d_i^2}{6\lambda_g Nu_i} \in [0.6, 1.5]\ s. \tag{94}$$

On the other hand, the particle-particle heat transfer time-scale can be rewritten as

$$\tau_{ik} = \frac{K}{h_{ik}}(2\Theta)^{-17/20}\ s \tag{95}$$

where K is a constant of order 250. Taking the upper-limit for the granular temperature of $\Theta = 10^{-2}$ gives $\tau_{ik} = 7000/h_{ik}\ s$. As h_{ik} is of the order 5 for this packing, $\tau_{ik} >> \tau_{gi}$ (even for this upper limit of granular temperature). The ratio τ_{ik}/τ_{gi} is even larger for lower granular temperatures. This analysis is, in principle, also valid for particle-wall collisions (except for a multiplicative constant arising from curvature differences). Considering the large ratio, τ_{ik}/τ_{gi}, the particle-particle heat transfer may be neglected in the regime where continuous frictional/rolling contacts prevail.

8 Appendix B: Calculation of collision integrals

The collision integrals for the source and flux contributions are

$$\chi_{ik}(\psi_i) = \sigma_{ik}^2 \int (\psi_i' - \psi_i)(\mathbf{g}\cdot\mathbf{k}) h_{ik} f_i f_k \left[1 + \frac{\sigma_{ik}}{2}\mathbf{k}\cdot\boldsymbol{\nabla}\ln\frac{f_k}{f_i}\right] d\mathbf{k}\, d\mathbf{c}_1 d\mathbf{c}_2 dm_1 dm_2 dT_1 dT_2 \tag{96}$$

$$\theta_{ik}(\psi_i) = -\frac{1}{2}\sigma_{ik}^3 \int \mathbf{k}(\psi_i' - \psi_i)(\mathbf{g}\cdot\mathbf{k}) h_{ik} f_i f_k \left[1 + \frac{\sigma_{ik}}{2}\mathbf{k}\cdot\boldsymbol{\nabla}\ln\frac{f_k}{f_i}\right] d\mathbf{k}\, d\mathbf{c}_1 d\mathbf{c}_2 dm_1 dm_2 dT_1 dT_2 \tag{97}$$

where the integration must be carried out over impending collisions ($\mathbf{g}\cdot\mathbf{k} \geq 0$). As mentioned in the main text, the single particle velocity distributions are Gaussians with their own temperature and mean velocity, and are assumed delta-peaked around the mean mass and temperature

$$f_i(\mathbf{c}, \mathbf{r}, t) = \frac{n_i}{(2\pi\Theta_i)^{3/2}} \exp[-\frac{(\mathbf{c} - \mathbf{u}_i)^2}{2\Theta_i}]\delta(m_i - \overline{m}_i)\delta(T_i - \widetilde{T}_i). \tag{98}$$

Note that the term in the integrand containing the gradient of the distribution functions can now be expressed in terms of gradients of the mean fields:

$$\begin{aligned}\boldsymbol{\nabla}\ln\left(\frac{f_k}{f_i}\right) &= -\boldsymbol{\nabla}\ln\left(\frac{n_i}{n_k}\right) + \frac{3}{2}\boldsymbol{\nabla}\ln\left(\frac{\Theta_i}{\Theta_k}\right) + \\ &\quad -\frac{1}{\Theta_i}\boldsymbol{\nabla}\mathbf{u}_i\cdot(\mathbf{c}_1 - \mathbf{u}_i) + \frac{1}{\Theta_k}\boldsymbol{\nabla}\mathbf{u}_k\cdot(\mathbf{c}_2 - \mathbf{u}_k) \\ &\quad -\frac{1}{2\Theta_i^2}(\mathbf{c}_1 - \mathbf{u}_i)^2\boldsymbol{\nabla}\Theta_i + \frac{1}{2\Theta_k^2}(\mathbf{c}_2 - \mathbf{u}_k)^2\boldsymbol{\nabla}\Theta_k.\end{aligned} \tag{99}$$

The most convenient way to calculate these integrals is to make a change of variables to $\mathbf{g} = \mathbf{c}_1 - \mathbf{c}_2$ and $\mathbf{c}_m = M_i\mathbf{c}_1 + M_k\mathbf{c}_2$. The Jacobian of the transformation equals unity

$$J = \frac{\partial(\mathbf{c}_1, \mathbf{c}_2)}{\partial(\mathbf{g}, \mathbf{c}_m)} = 1/\frac{\partial(\mathbf{g}, \mathbf{c}_m)}{\partial(\mathbf{c}_1, \mathbf{c}_2)} = 1/(M_i + M_k) = 1. \tag{100}$$

Through this transformation the integrals become

$$\begin{aligned}\chi_{ik}(\psi_i) &= \sigma_{ik}^2 h_{ik}\frac{n_i n_k}{(4\pi^2\Theta_i\Theta_k)^{3/2}} \int (\psi_i' - \psi_i)(\mathbf{g}\cdot\mathbf{k}) \left[1 + \frac{\sigma_{ik}}{2}\mathbf{k}\cdot\boldsymbol{\nabla}\ln\frac{f_k}{f_i}\right] \times \\ &\quad exp\{-\frac{1}{2\Theta_g}(\mathbf{g} - \Delta\mathbf{u}_{ik})^2 - \frac{1}{2\Theta_{ik}}(\mathbf{c}_m - \mathbf{u}_0)^2\} d\mathbf{k}\, d\mathbf{c}_m d\mathbf{g}\end{aligned} \tag{101}$$

$$\begin{aligned}\theta_{ik}(\psi_i) &= -\frac{1}{2}\sigma_{ik}^3 h_{ik}\frac{n_i n_k}{(4\pi^2\Theta_i\Theta_k)^{3/2}} \int \mathbf{k}(\psi_i' - \psi_i)(\mathbf{g}\cdot\mathbf{k}) \left[1 + \frac{\sigma_{ik}}{2}\mathbf{k}\cdot\boldsymbol{\nabla}\ln\frac{f_k}{f_i}\right] \times \\ &\quad exp\{-\frac{1}{2\Theta_g}(\mathbf{g} - \Delta\mathbf{u}_{ik})^2 - \frac{1}{2\Theta_{ik}}(\mathbf{c}_m - \mathbf{u}_0)^2\} d\mathbf{k}\, d\mathbf{c}_m d\mathbf{g}\end{aligned} \tag{102}$$

where the integration over m_1, m_2, T_1, and T_2 have already been carried out and the terms in the integrand $\psi_i' - \psi_i$ and $\boldsymbol{\nabla} \ln(f_k/f_i)$ must be expressed in the integration variables. For convenience, the following parameters have been introduced

$$\begin{aligned} \Theta_g &= \Theta_i + \Theta_k \\ \frac{1}{\Theta_{ik}} &= \frac{1}{\Theta_i} + \frac{1}{\Theta_k}, \quad \Theta_{ik} = \frac{\Theta_i \Theta_k}{\Theta_i + \Theta_k} \\ \Delta\mathbf{u}_{ik} &= \mathbf{u}_i - \mathbf{u}_k \\ \mathbf{u}_0 &= \mathbf{u}_m + a_0 \mathbf{g} \\ \mathbf{u}_m &= (\frac{\mathbf{u}_i}{\Theta_i} + \frac{\mathbf{u}_k}{\Theta_k})\Theta_{ik} \\ \mathbf{a}_0 &= (M_i\Theta_i - M_k\Theta_k)/\Theta_g. \end{aligned} \tag{103}$$

The integrals over $\mathbf{k}$ and $\mathbf{c}_m$ are standard, and can be done with the help of standard integral tables (see Chapman and Cowling, 1970 and Jenkins and Richman, 1985). The integrals over $\mathbf{g}$ are, however, very cumbersome to perform, at least for general $\Delta\mathbf{u}_{ik}$. These integrals are of the general form

$$I = \int N(\mathbf{g}) exp\{-\frac{1}{2\Theta_g}(\mathbf{g} - \Delta\mathbf{u}_{ik})^2\} d\mathbf{g}. \tag{104}$$

Introducing the dimensionless variable $z = \frac{1}{2\Theta_g}\Delta\mathbf{u}_{ik}{}^2$, the integrals have a polynomial form in z combined with exponentials and errorfunctions. To avoid this algebraic complexity and since the relative velocity is generally small in dense beds, the integrals are approximated for small z (or small $\Delta\mathbf{u}_{ik}$). It is thus legitimate to expand the integrals in a Taylor series around $z = 0$ and retain the lowest orders in z. Recently, Gourdel et al. (2000) have calculated several collision integrals for general z, however, they only required the source terms in the case of homogeneous flows (no gradient integrals needed to be included). The integrals, calculated using the small z approximation, properly reduce to those of Jenkins and Mancini (1987) calculated in the limit of small drift and small temperature differences.

9 Appendix C: Derivation of the self-diffusion coefficient

The diffusive flux associated with fluctuations in particle velocity and a general variable Ψ reads $-\nabla \cdot (\alpha_i \overline{\rho}_i < \mathbf{C}_i \Psi_i' >)$. As the distribution for Ψ is unknown, we use mean free path theory to obtain a reasonable estimate of this flux (Chapman and Cowling, 1970). Following Chapman and Cowling we have

$$- < \mathbf{C}_i \Psi_i' > \approx \frac{1}{2} \overline{C}_i l_i \nabla \Psi_i$$

where $\overline{C}_i$ is the average magnitude of C_i and l_i denotes the mean free path of particles in class i. Comparing this formulation with the original flux, we deduce the diffusion coefficient as

$$D_{ii} = \frac{1}{2} \overline{C}_i l_i$$

For a Gaussian distribution the average magnitude of the fluctuating velocity reads $\overline{C}_i = (8\Theta_i/\pi)^{1/2}$, while an expression for the mean free path in a dense binary suspension is given in Hsiau (2000). The above diffusion coefficient is only valid when the dynamics of the particle evolves relatively slow between collisions, i.e. $d\Psi/dt \approx 0$, i.e. the timescale for collisions is much smaller than a characteristic timescale for particle dynamics. For dense systems, this condition is likely to be satisfied. Hsiau (2000) recently presented an analysis for heat conduction in granular flows where this assumption is relaxed.

References

[1] Anderson, K. G. and Jackson, R., 1992. A comparison of the solutions of some proposed equations of motion of granular materials for fully developed flow down inclined planes. J. Fluid Mech. 241, 145-168.

[2] Balzer, G., Boelle, A., Simonin, O., 1995. Eulerian gas-solid flow modelling of dense fluidized bed. FLUIDIZATION VIII, Proc. International Symposium of the Engineering Foundation, 1125-1134.

[3] Barrett, R., Berry, M., Chan, T. F., Demmel, J., Donato, J., Dongarra, J., Eijkhout, V., Pozo, R., Romine, C., and Van der Vorst, H., 1994. Templates for the solution of linear systems: building blocks for iterative methods. SIAM, Philedelphia.

[4] Bird, R. B., Stewart, W. E. and Lightfoot, E. N. 1960. Transport Phenomena, Wiley.

[5] Boemer, A. and Renz, U., 1997. Eulerian simulation of bubble formation at a jet in a two-dimensional fluidized bed. Int. J. Multiphase Flow. 21(5), 927-944.

[6] Campbell, C. S., 1990. Rapid granular flows. Ann. Rev. Fluid Mech. 22, 57-92.

[7] Campbell, C. S. and Wang, D. G., 1991. Particle pressures in gas-fluidized beds. J. Fluid Mech. 227, 495-508.

[8] Chapman, S. and Cowling, T. G., 1970. The Mathematical Theory of Nonuniform Gases. Cambridge University Press.

[9] CRC handbook of chemistry and physics. 1992. CRC Press Inc.

[10] Di Felice, R., Coppola, G., Rapagna, S., and Jand, N.,1999. Modeling of biomass devolatilization in a fluidized bed reactor. The Can. J. Chem. Eng. 77, 325-332.

[11] Drew, D. A., 1983. Mathematical modeling of two-phase flow. Ann. Rev. Fluid Mech.15:261-291.

[12] Farell, M., Lun, C. K. K and Savage, S. B., 1986. A simple kinetic theory for granular flow of binary mixtures of smooth, inelastic, spherical particles. Acta Mechanica 63, 45-60.

[13] Goldhirsch, I., 1999. Scales and kinetics of granular flows. Chaos 9(3), 659-672.

[14] Goldman, E. and Sirovich, L., 1967. Equations for gas mixtures. Phys. Fluids 10, 1928-1940.

[15] Gourdel, C., Simonin, O. and Brunier, E., 2000. Eulerian Modelling of binary mixtures of colliding particles and validation from Lagrangian tracking coupled to Large Eddy Simulation of homogeneous gas-solid turbulent flow. Submitted to Int. J. Multiphase Flow.

[16] Grad, H., 1949. On the kinetic theory of rarified gases. Comm. Pure and Appl. Math. 2, 331-407.

[17] Gunn, D. J., 1978. Transfer of heat or mass to particles in fixed and fluidized beds. Int. J. Heat Mass Transfer 21, 467-476.

[18] Gyarmathy, G., 1982. The spherical droplet in gaseous carrier streams: review and synthesis. In: Multiphase science and technology, Vol. 1. Eds. Hewitt, G. F., Delhaye, J. M., and Zuber, N. McGraw Hill, 99-279.

[19] Brown, P. N., Byrne, G. D. and Hindmarsh, A. C., 1989. VODE: A Variable-coefficient ODE solver. SIAM J. Sci. Stat. Comput. 10(5), 1038-1051.

[20] Hsiau, S. S., 2000. Effective Thermal Conductivities of a Single Species and a Binary Mixture of Granular Materials. Int. Journal Multiph. Flow, 387-419.

[21] Jenkins, J. T. and Savage, S. B., 1983. A theory for the rapid flow of identical, smooth, nearly elastic, spherical particles. J. Fluid Mech. 130, 187-202.

[22] Jenkins, J. T. and Richman, M. W., 1985. Grad's 13-moment system for a dense gas of inelastic spheres. Arch. Ration. Mech. Anal. 87, 355-377.

[23] Jenkins, J. T. and Mancini, F., 1987. Balance laws and constitutive relations for plane flows of a dense, binary mixture of smooth, nearly elastic, circular disks. Journal of Applied Mechanics 54, 27-34.

[24] Jenkins, J. T. and Mancini, F., 1989. Kinetic theory for binary mixtures of smooth, nearly elastic spheres. Phys. Fluids A 1(12), 2050-2057.

[25] Johnson, P. C. and Jackson, R., 1987. Frictional-collisional constitutive relations for granular materials, with application to plane shearing. J. Fluid Mech. 176, 67-93.

[26] Johnsson, F., Andersson, S., and Leckner, B., 1991. Expansion of a freely bubbling fluidized-bed. Powder Technology 68(2), 117-123.

[27] Valiveti, P. and Koch, D. L., 1998. Instability of sedimenting bidisperse particle gas suspensions. Appl. Sci. Res. 58, 275-303.

[28] Kumaran, V. and Koch, D. L., 1993a. Properties of a bidisperse particle-gas suspension Part 1. Collision time small compared with viscous relaxation time. J. Fluid. Mech. 247, 623-641.

[29] Kumaran, V. and Koch, D. L., 1993b. Properties of a bidisperse particle-gas suspension Part 2. Viscous relaxation time small compared with collision time. J. Fluid. Mech. 247, 643-660.

[30] Lathouwers, D., 1999. Modelling and Simulation of Bubbly Flows. PhD thesis, Delft Univeristy of Technology, The Netherlands.

[31] Lathouwers, D. and Bellan, J., 1999. Fall Technical Meeting of the Western States Section of the Combustion Institute, Irvine, October 25-26.

[32] Lathouwers, D. and Bellan, J., 2000a. Modeling and simulation of bubbling fluidized beds containing particle mixtures. Proceedings of the Combustion Institute, Vol. 28, in print.

[33] Lathouwers, D. and Bellan, J., 2000b. Yield optimization and scaling of fluidized beds for tar production from biomass. In preparation for Energy and Fuels.

[34] Louge, M., Yusof, J. M. and Jenkins, J. T., 1993. Heat transfer in the pneumatic transport of massive particles. Int. J. Heat Mass Transfer 36(2), 265-275.

[35] Lun, C. K. K., Savage, S. B., Jeffrey, D. J. and Chepurniy, N., 1984. Kinetic theories for granular flow: inelastic particles in Couette flow and slightly inelastic particles in a general flowfield. J. Fluid Mech. 140, 223-256.

[36] Ma, D., Eraslan, A. H. and Ahmadi, G., 1993. A computer code for analyzing transient three-dimensional rapid granular flows in complex geometries. Computers & Fluids 22(1), 25-50.

[37] Mathiesen, V., Solberg, T. and Hjertager, B. H., 2000. An experimental and computational study of multiphase flow behavior in a circulating fluidized bed. Int. J. Multiphase Flow 26, 83-97.

[38] Miller, R. S. and Bellan, J., 1997. A generalized biomass pyrolysis model based on superimposed cellulose, hemicellulose and lignin kinetics. Combust. Sci. and Tech. 126, 97-137.

[39] Miller, R. S. and Bellan, J., 1998. Numerical simulation of vortex pyrolysis reactors for condensable tar production from biomass. Energy and Fuels 12(1), 25-40.

[40] Miller, R. S., Harstad, K. and Bellan, J., 1999. Evaluation of equilibrium and non-equilibrium evaporation models for many-dropletgas-liquid flow simulations. Int. J. Multiphase Flow 24(6), 1025-1055.

[41] Ottino, J. M. and Khakhar, D. V., 2000. Mixing and segegation of granular materials. Ann. Rev. Fluid Mech. 32, 55-91.

[42] Peirano, E. and Leckner, B., 1998. Fundamentals of turbulent gas-solid flows applied to circulating fluidized bed combustion. Prog. Energy Combust. Sci. 24, 259-296.

[43] Savage, S. B. and Sayed, M., 1984. Stresses developed by dry cohesionless granular materials sheared in an annular shear cell. J. Fluid Mech. 142, 391-430.

[44] Schiller, L. and Nauman, A., 1935. A drag coefficient correlation. V.D.I. Zeitung, 77, 318-320.

[45] Scott, D. S. and Piskorz, J., 1982. The flash pyrolysis of Aspen-polar wood. Can. Journal Chem Eng. 60, 666-674.

[46] Scott, D. S. and Piskorz, J., 1984. The continuous pyrolysis of biomass. Can. Journal Chem Eng. 62, 404-412.

[47] Scott, D. S., Majerski, P., Piskorz, J., and Radlein, D., 1984. A second look at fast pyrolysis of biomass - the RTI process. J. Anal. Appl. Pyrolysis 51, 23-37.

[48] Simonin, O., 1996. Combustion and turbulence in two-phase flows. Von Karman Lecture Series 1996-02, Von Karman Institute for Fluid Dynamics.

[49] Strang, G., 1968. On the construction and comparison of difference schemes. SIAM J. of Numer. Anal. 5(3), 506.

[50] Syamlal, M., 1993. MFIX Documentation Theory Guide. DOE Report No. DOE/METC-94/1004.

[51] Sun, J. and Chen, M. M., 1988. A theoretical analysis of heat transfer due to particle impact. Int. J. Heat Mass Transfer 31(5), 969-975.

[52] Tham, M. K. and Gubbins, K. E., 1971. Kinetic theory of multicomponent dense fluid mixtures of rigid spheres. J. Chem. Phys. 55(1), 268-279.

[53] Young, J. B., 1995. The fundamental equations of gas-droplet flow. Int. J. Multiphase Flow 21(2), 175-191.

[54] Zamankhan, P., 1995. Kinetic theory of multicomponent dense mixtures of slightly inelastic spherical particles. Phys. Rev. E 52(5), 4877-4891.

Reaction	$A(1/s)$	$E(J/kmol)$
K_1^c	$2.8 \cdot 10^{19}$	$242.4 \cdot 10^6$
K_2^c	$3.28 \cdot 10^{14}$	$196.5 \cdot 10^6$
K_3^c	$1.30 \cdot 10^{10}$	$150.5 \cdot 10^6$
K_1^h	$2.10 \cdot 10^{16}$	$186.7 \cdot 10^6$
K_2^h	$8.75 \cdot 10^{15}$	$202.4 \cdot 10^6$
K_3^h	$2.60 \cdot 10^{11}$	$145.7 \cdot 10^6$
K_1^l	$9.60 \cdot 10^8$	$107.6 \cdot 10^6$
K_2^l	$1.50 \cdot 10^9$	$143.8 \cdot 10^6$
K_3^l	$7.70 \cdot 10^6$	$111.4 \cdot 10^6$
K_4	$4.28 \cdot 10^6$	$108 \cdot 10^6$

Table 1: Rate constants and activation energy for the biomass pyrolysis kinetics scheme. The char formation ratios for reaction K_3 are: $X^c = 0.35$, $X^h = 0.60$, and $X^l = 0.75$.

Specie	$W(kg/kmol)$	$C_p(J/kgK)$	$\lambda(J/msK)$	$\mu(kg/ms)$	$D(m^2/s)$
N_2	28.013	1120.91	$5.63 \cdot 10^{-2}$	$3.58 \cdot 10^{-5}$	$8.52 \cdot 10^{-4}$
Gas	30	1100	$2.577 \cdot 10^{-2}$	$3.0 \cdot 10^{-5}$	$1.1 \cdot 10^{-4}$
Tar	100	2500	$2.577 \cdot 10^{-2}$	$3.0 \cdot 10^{-5}$	$1.1 \cdot 10^{-4}$

Table 2: Property values for the gas phase species. The properties for nitrogen are taken at $T = 800K$ and $p = 100kPa$.

Species	$C_p (J/kgK)$	$\rho (kg/m^3)$
Biomass	2167	2300
Char	2333	1100
Sand	800	2600

Table 3: Specific heat and densities for solid species. Biomass refers to both virgin species and active species.

Feed	cellulose	hemicellulose	lignin
bagasse	0.36	0.47	0.17
olive husk	0.22	0.33	0.45
maple	0.40	0.38	0.22
oak	0.35	0.40	0.25

Table 4: Initial biomass composition by mass fractions (cf. Miller and Bellan, 1997).

Run No	$T_g (K)$	$T_b (K)$	Feedpoint	Feedstock	Fluidflow(kg/m^2s)
1	600	400	1	bagasse	0.3
2	700	400	1	bagasse	0.3
3	750	400	1	bagasse	0.3
4	800	400	1	bagasse	0.3
5	850	400	1	bagasse	0.3
6	950	400	1	bagasse	0.3
7	750	450	1	bagasse	0.3
8	750	500	1	bagasse	0.3
10	750	400	1	bagasse	0.4
12	750	400	1	olive husk	0.3
13	750	400	1	maple	0.3
14	750	400	1	oak	0.3
16	750	400	1+2	bagasse	0.3

Table 5: Summary of operating parameters in the simulations performed.

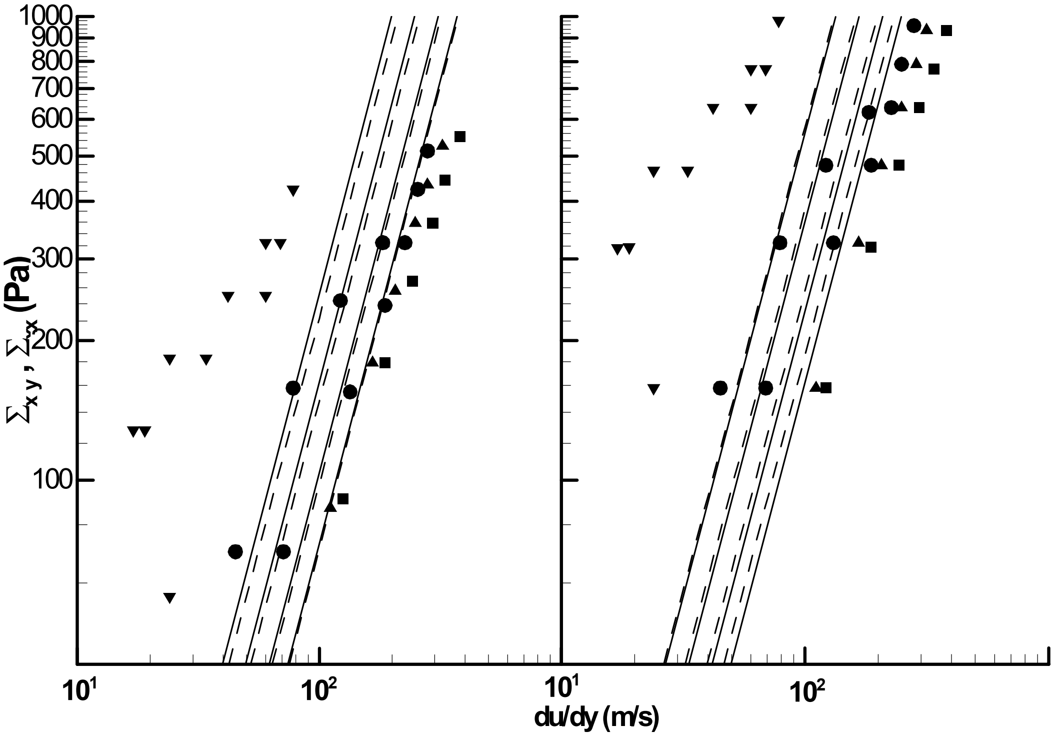

Figure 1: Predictions of the total shear (left) and normal stresses (right) generated in a simple shear flow of a binary mixture as function of shear rate for various bulk solids fractions, compared with the experimental data from Savage and Sayed (1984). Predictions: —— binary model, - - - -, monodisperse model. Experimental data: ■: $\alpha_{tot} = 0.498$, ▲: $\alpha_{tot} = 0.512$, •: $\alpha_{tot} = 0.528$, ▼: $\alpha_{tot} = 0.542$.

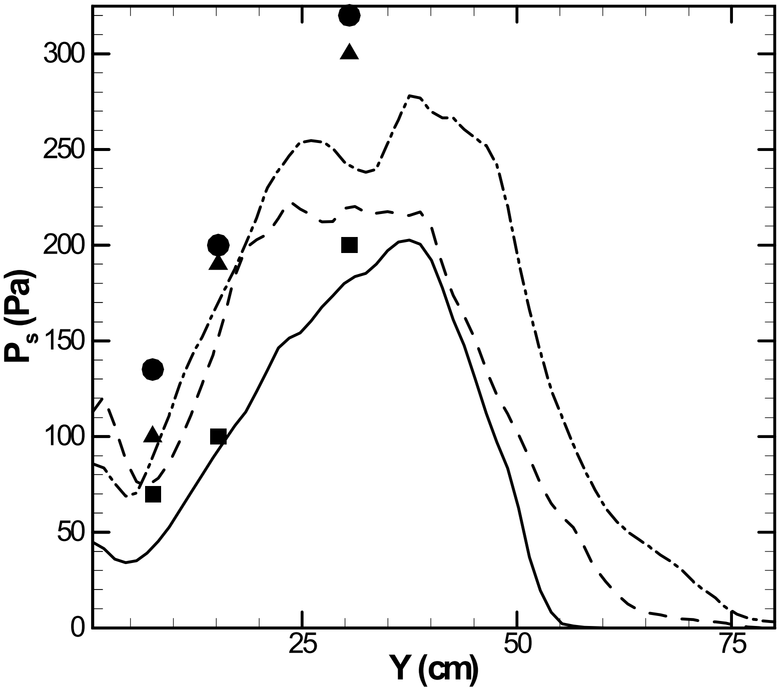

Figure 2: Predictions of the total time-averaged solids pressure along the wall compared to experimental data of Campbell and Wang (1991) at different superficial gas velocities. Predictions: $V_g = 0.4$: —; $V_g = 0.6$: - - - ; $V_g = 0.8$:–·–, Experimental data: $V_g = 0.4$: ■; $V_g = 0.6$: , ▲; $V_g = 0.8$: ●.

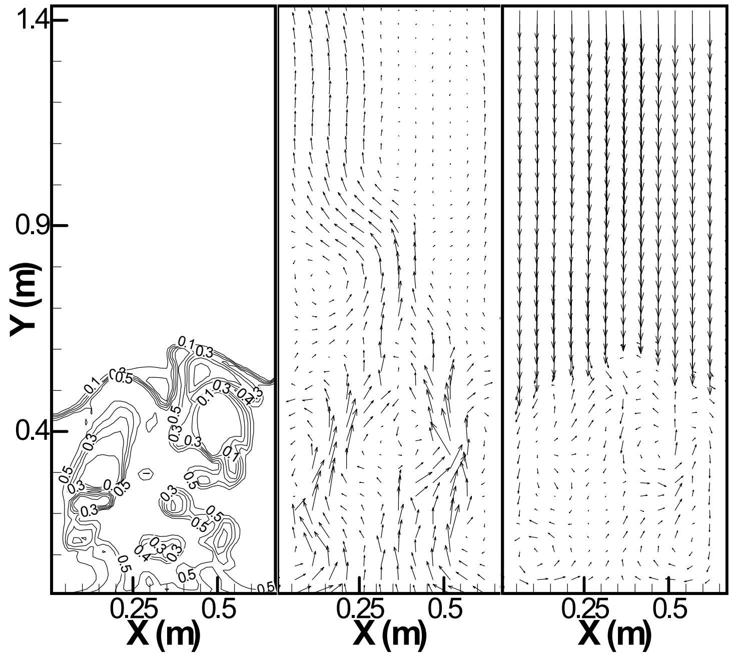

Figure 3: Instantaneous fields of the solid phase fraction (left), gas velocity (middle) and solids velocity (right) at $t = 3s$. (only 1 out of every 9 velocity vectors is shown).

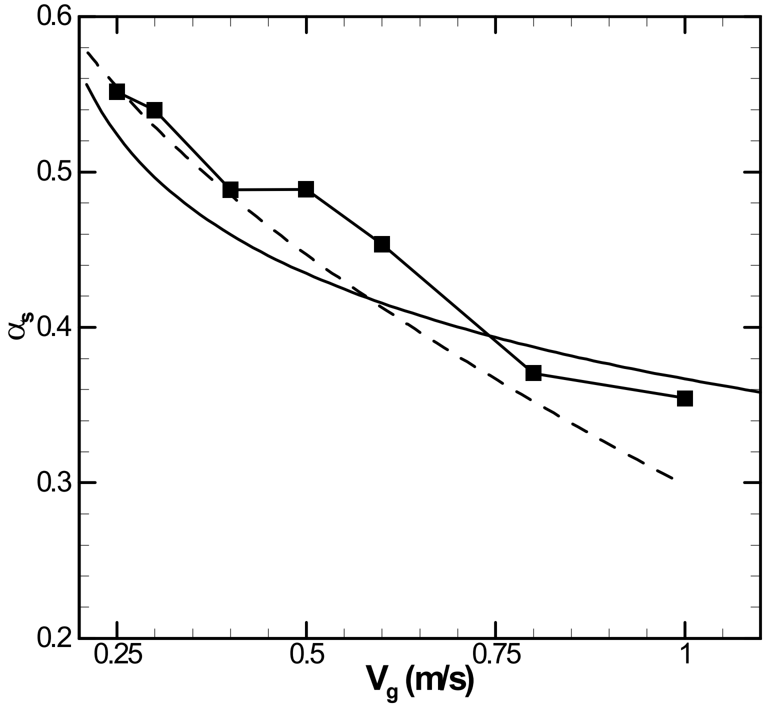

Figure 4: Solid phase volume fraction in the lower bed as function of the superficial gas velocity: ■ present model, —— experimental correlation of Johnsson et al. (1991), - - - equilibrium solution of two-fluid equations.

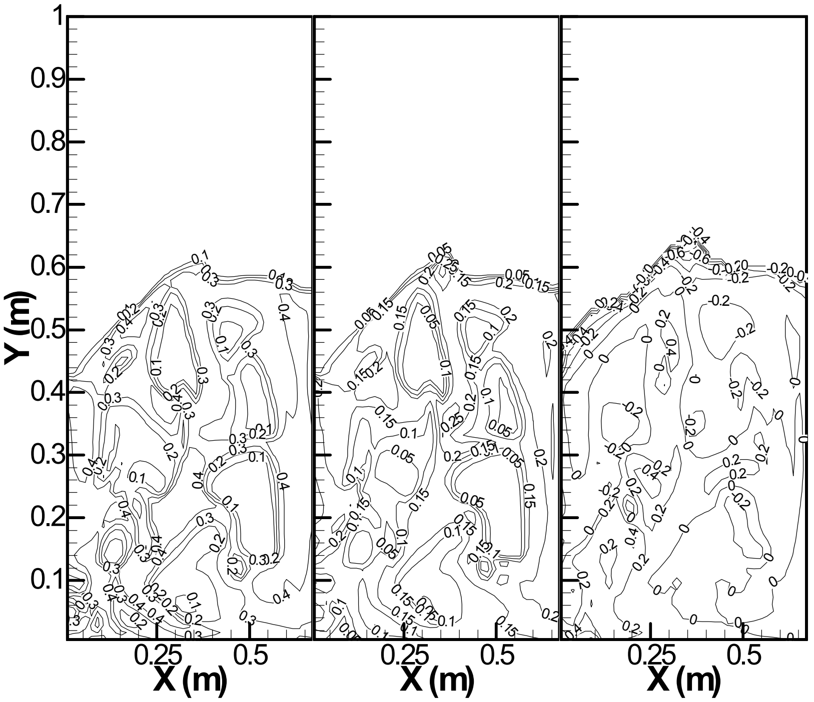

Figure 5: Instantaneous distributions of sand (left) and biomass (middle) concentrations, and of the segregation parameter (right) at $t = 6s$.

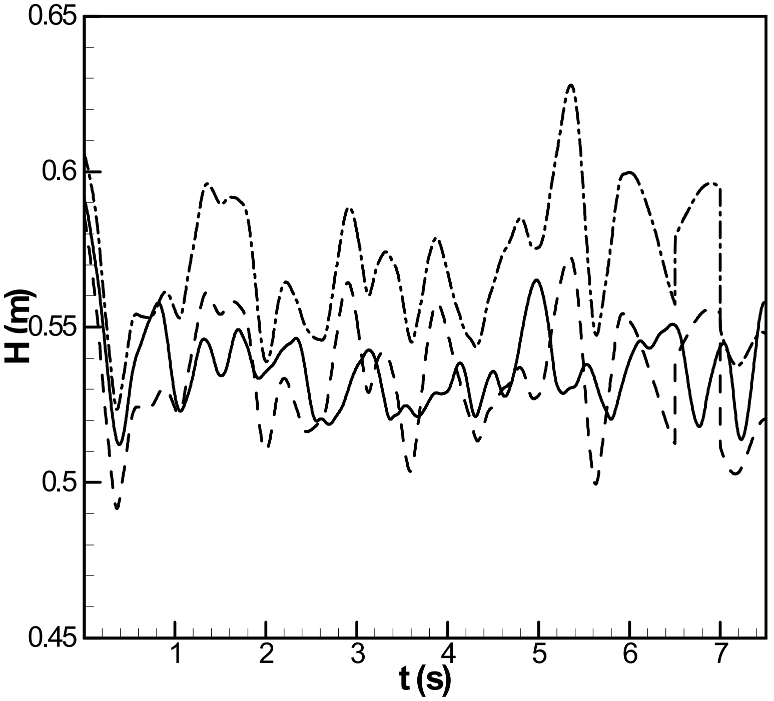

Figure 6: Time evolution of the y-coordinate of center of mass of sand and biomass compared to that of a monodispersed simulation: monodisperse:—–, sand: - - - ; biomass: –·–.

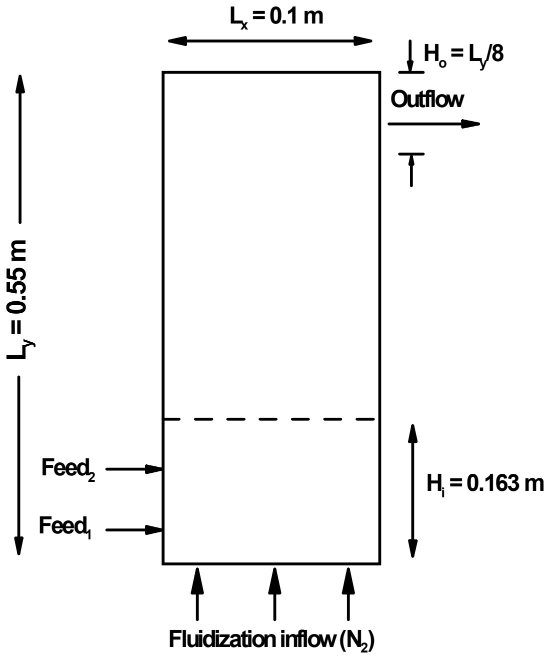

Figure 7: Schematic of the fluidized bed reactor.

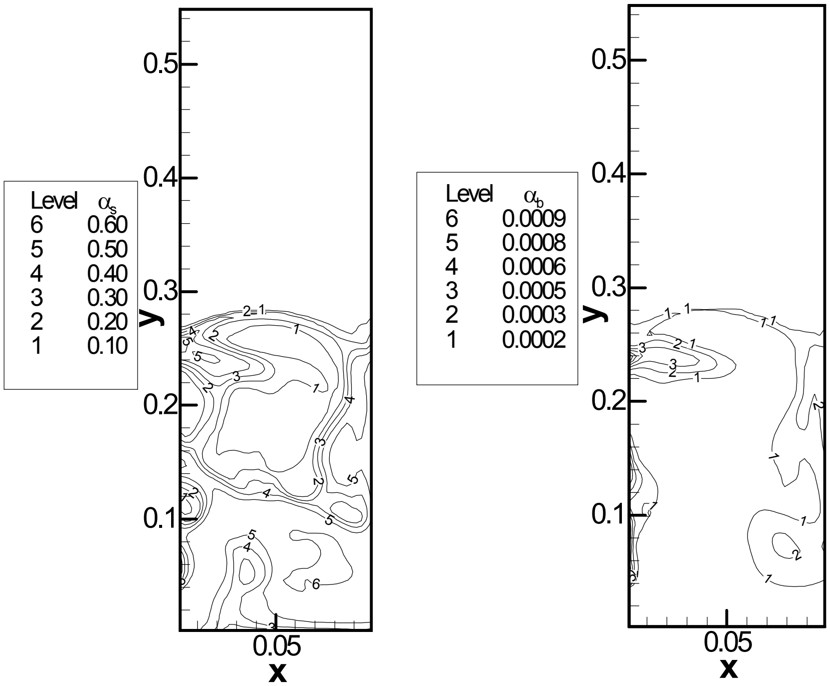

Figure 8: Contours of the volume fractions of sand (left) and biomass (right) at t=2.5 s.

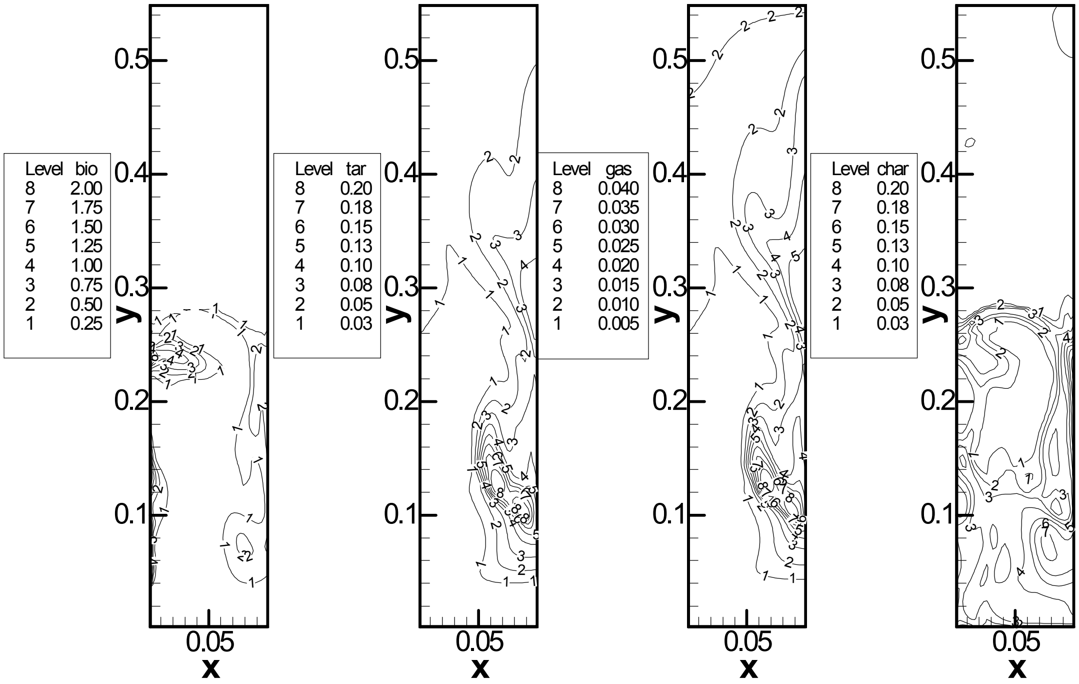

Figure 9: Contours of partial density of biomass, tar, gas and char at t=2.5 s.

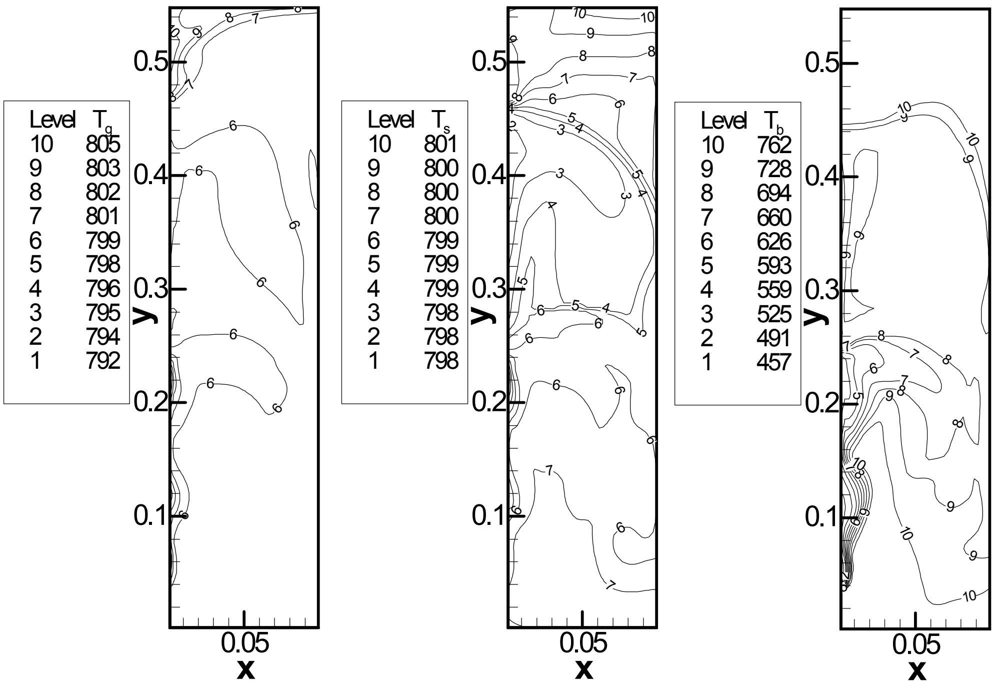

Figure 10: Contours of the temperatures of the gas (left), sand (middle), and biomass (right) at t=2.5 s.

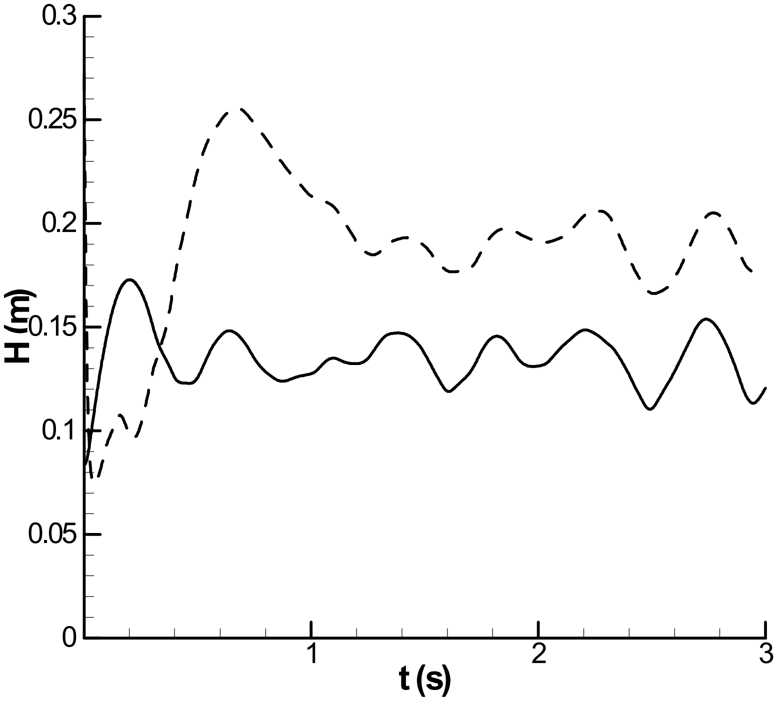

Figure 11: Averaged vertical coordinate of center of mass of sand (——) and biomass (- - - - -) particles in the reactor. Data reflect case no 4.

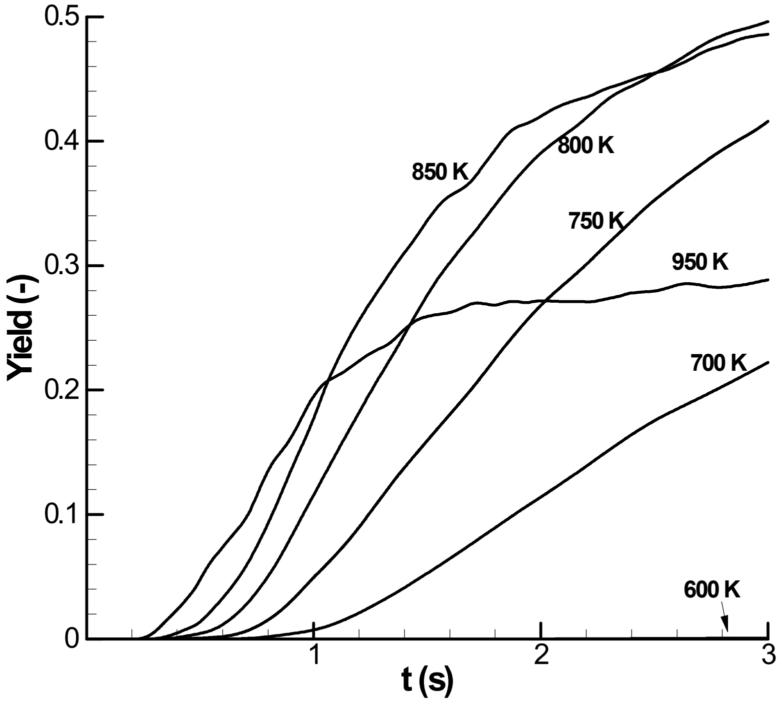

Figure 12: Tar yield as function of time for various gas temperatures; otherwise standard conditions.

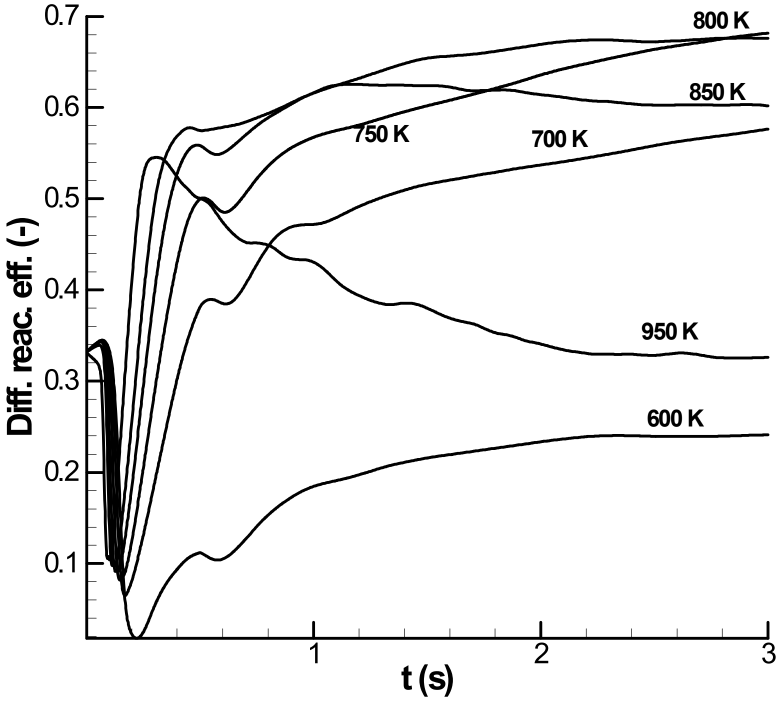

Figure 13: Tar differential reactor efficiency as function of time for various gas temperatures; otherwise standard conditions.

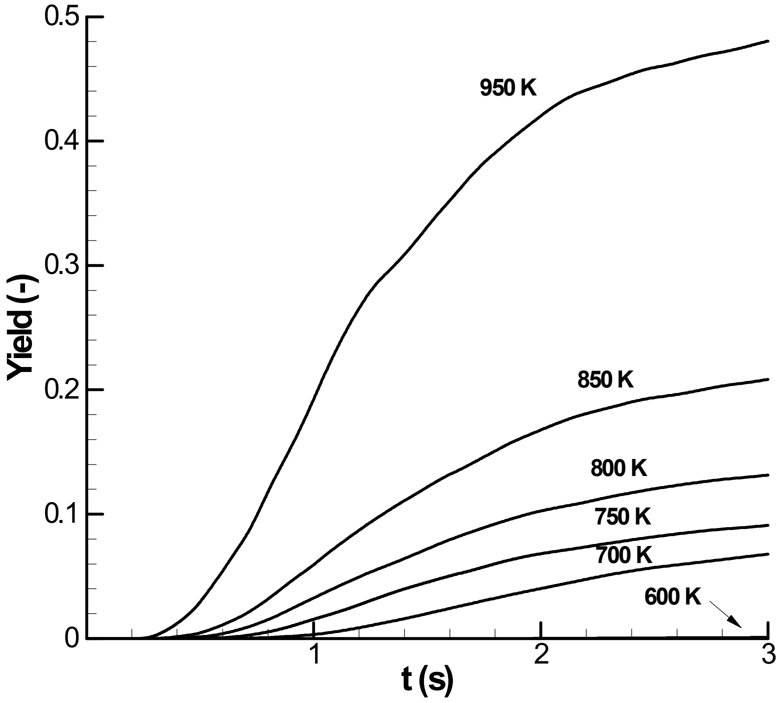

Figure 14: Gas yield as function of time for various gas temperatures; otherwise standard conditions.

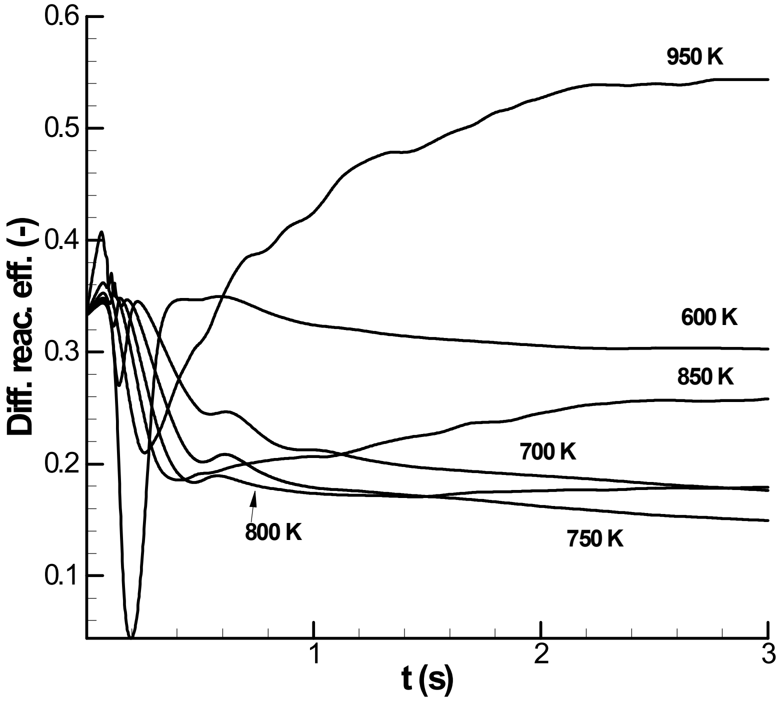

Figure 15: Gas differential reactor efficiency as function of time for various gas temperatures; otherwise standard conditions.

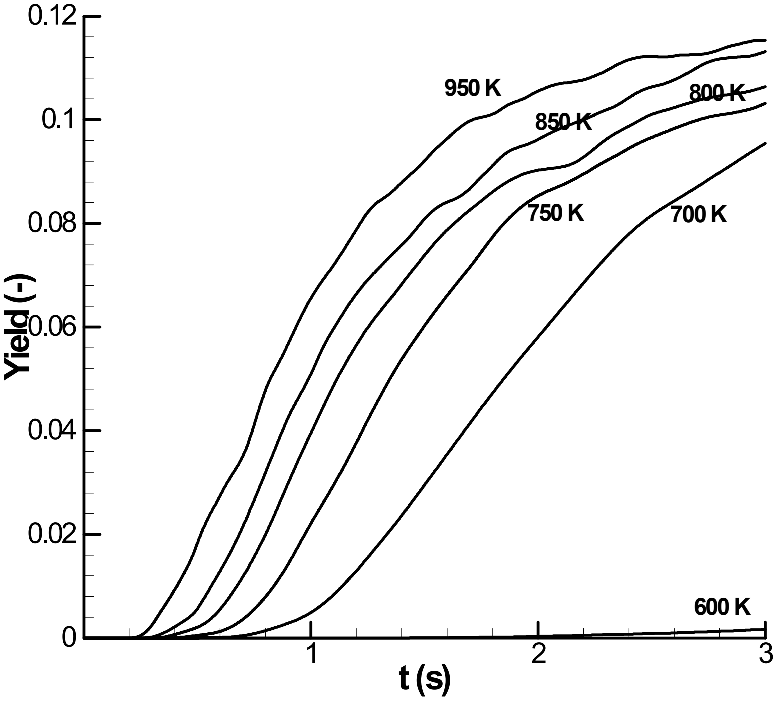

Figure 16: Char yield as function of time for various gas temperatures; otherwise standard conditions.

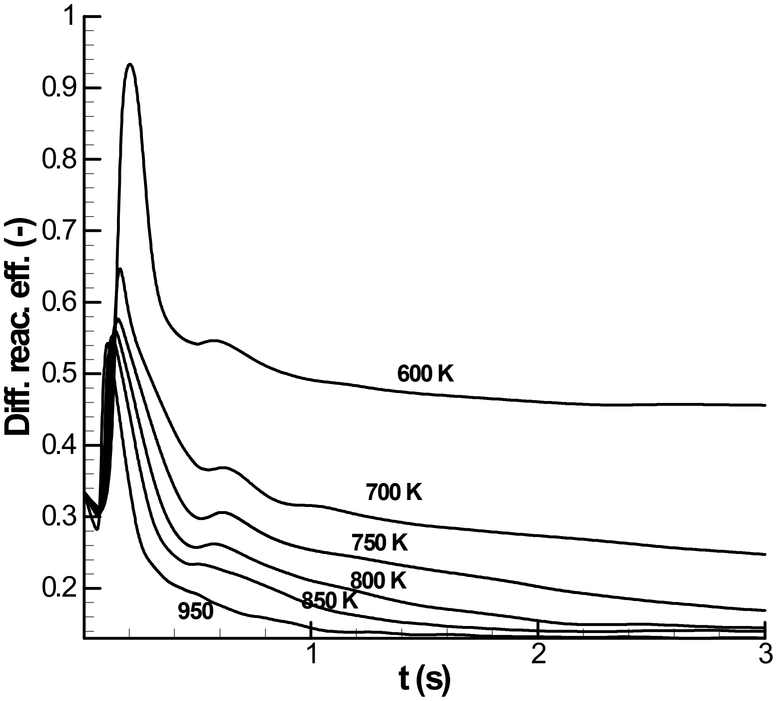

Figure 17: Char differential reactor efficiency as function of time for various gas temperatures; otherwise standard conditions.

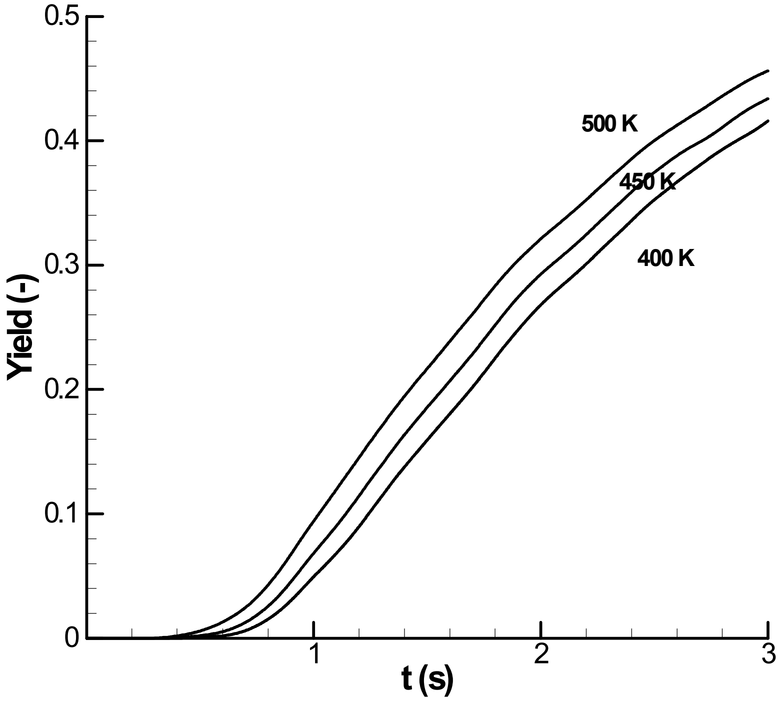

Figure 18: Tar yield as function of time for various biomass feed temperatures; otherwise standard conditions.

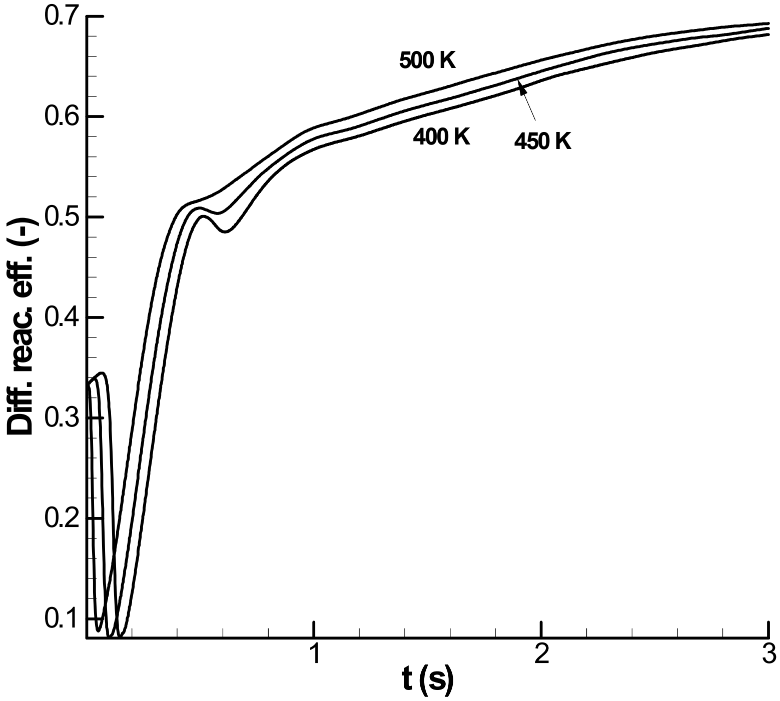

Figure 19: Tar differential reactor efficiency as function of time for various biomass feed temperatures; otherwise standard conditions.

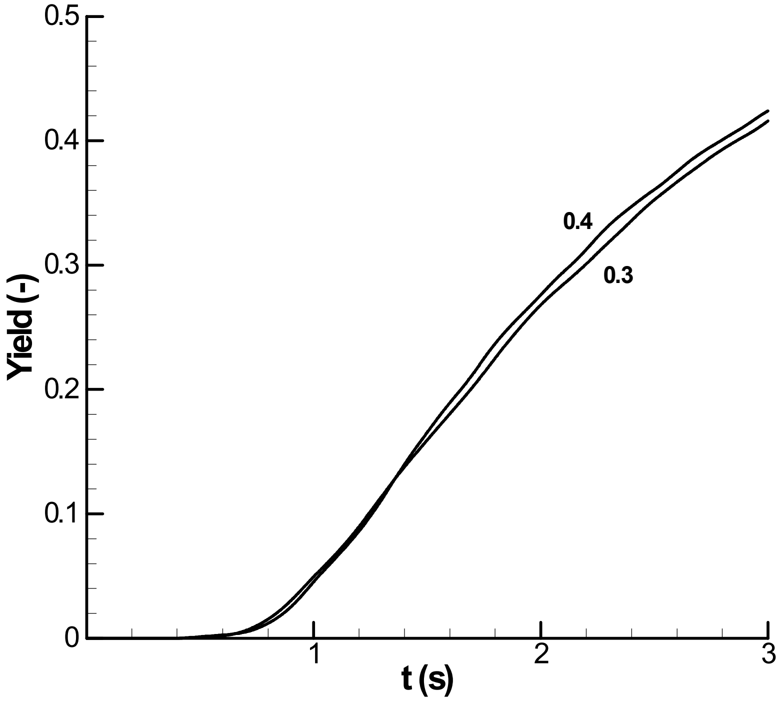

Figure 20: Tar yield as function of time for different fluidization fluxes; otherwise standard conditions.

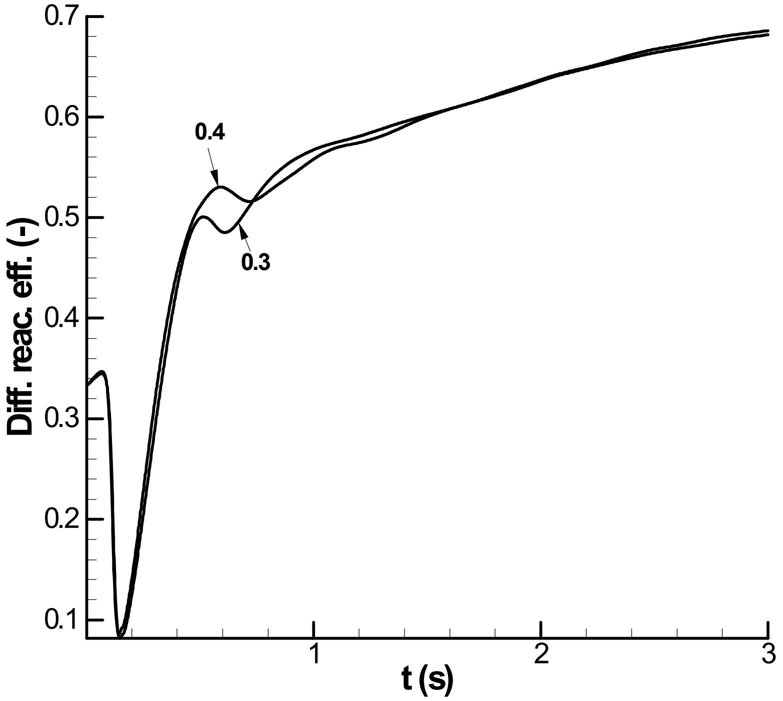

Figure 21: Tar differential reactor efficiency as function of time for different fluidization fluxes; otherwise standard conditions.

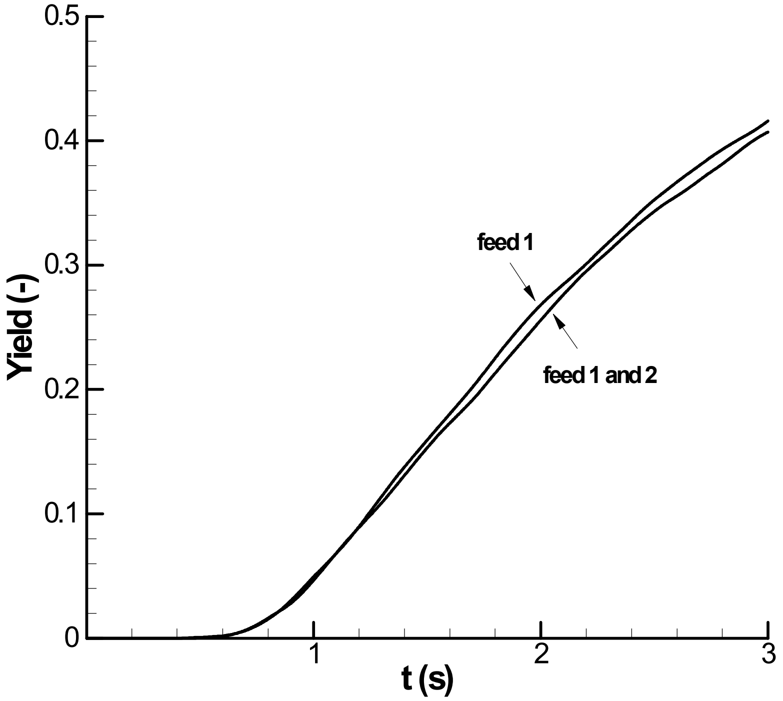

Figure 22: Tar yield as function of time for different feedpoint configurations; otherwise standard conditions.

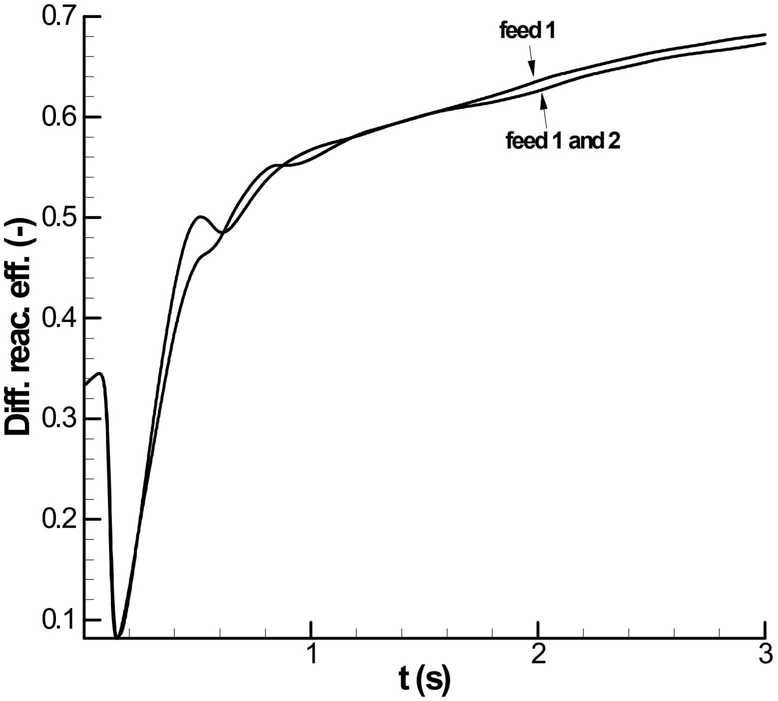

Figure 23: Tar differential reactor efficiency as function of time for different feedpoint configurations; otherwise standard conditions.

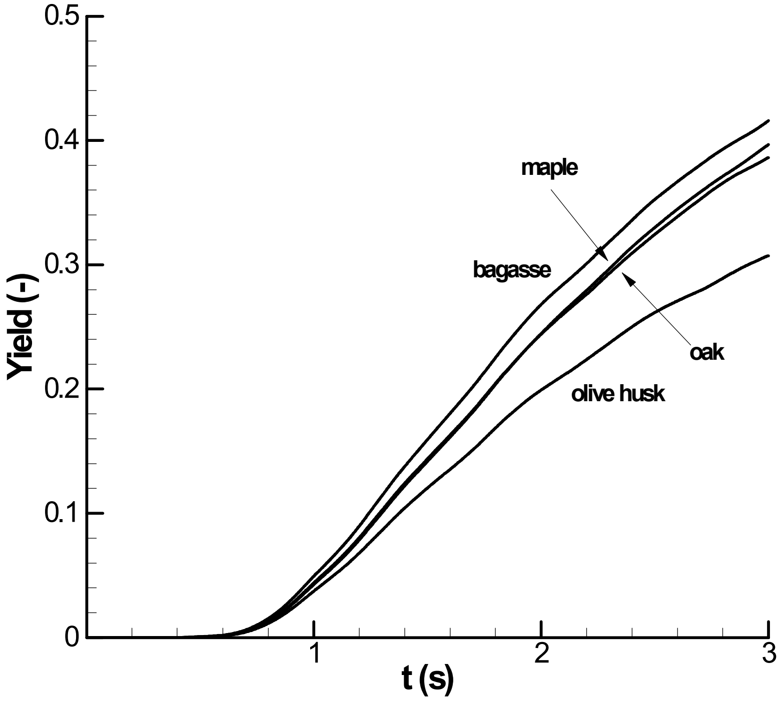

Figure 24: Tar yield as function of time for various biomass feedstock; otherwise standard conditions.

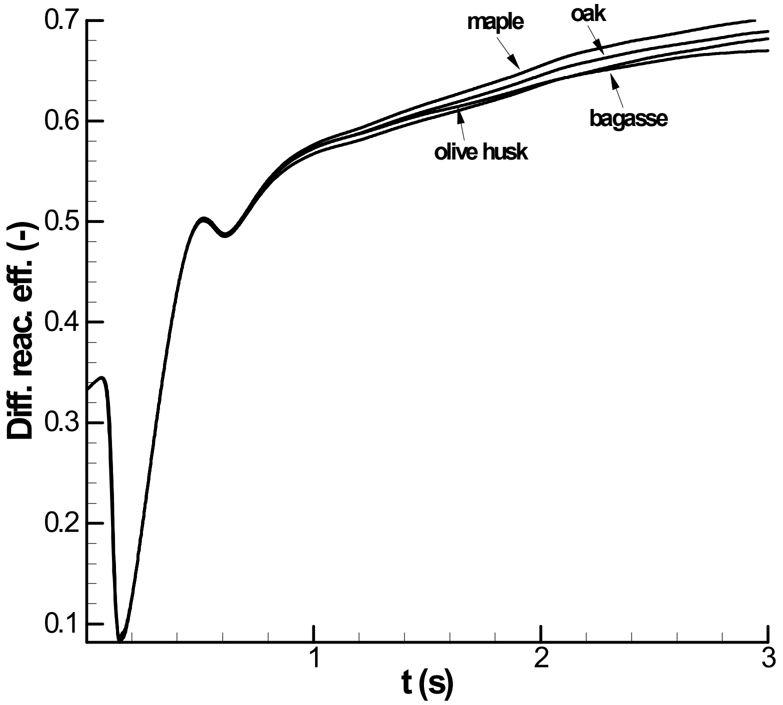

Figure 25: Tar differential reactor efficiency as function of time for various biomass feedstock; otherwise standard conditions.